J. Fluid Mech. (1995), *vol.* 282, *pp.* 247–278
Copyright © 1995 Cambridge University Press

Axial drop motion in rotating fluids

By J. W. M. BUSH[1]†, H. A. STONE[2] AND J. BLOXHAM[1]

[1] Department of Earth and Planetary Sciences, Harvard University, Cambridge, MA 02138, USA

[2] Division of Applied Sciences, Harvard University, Cambridge, MA 02138, USA

(Received 16 August 1993 and in revised form 28 March 1994)

A theoretical and experimental investigation of drop motion in rotating fluids is presented. The theory describing the vertical on-axis translation of an axisymmetric rigid body through a rapidly rotating low-viscosity fluid is extended to the case of a buoyant deformable fluid drop of arbitrary viscosity. In the case that inertial and viscous effects are negligible within the bulk external flow, motions are constrained to be two-dimensional in compliance with the Taylor–Proudman theorem, and the rising drop is circumscribed by a Taylor column. Calculations for the drop shape and rise speed decouple, so that theoretical predictions for both are obtained analytically. Drop shapes are set by a balance between centrifugal and interfacial tension forces, and correspond to the family of prolate ellipsoids which would arise in the absence of drop translation. In the case of a drop rising through an unbounded fluid, the Taylor column is dissipated at a distance determined by the outer fluid viscosity, and the rise speed corresponds to that of an identically shaped rigid body. In the case of a drop rising through a sufficiently shallow plane layer of fluid, the Taylor column extends to the boundaries. In such bounded systems, the rise speed depends further on the fluid and drop viscosities, which together prescribe the efficiency of the Ekman transport over the drop and container surfaces.

A set of complementary experiments is also presented, which illustrate the effects of drop viscosity on steady drop motion in bounded rotating systems. The experimental results provide qualitative agreement with the theoretical predictions; in particular, the poloidal circulation observed inside low-viscosity drops is consistent with the presence of a double Ekman layer at the interface, and is opposite to that expected to arise in non-rotating systems. The steady rise speeds observed are larger than those predicted theoretically owing to the persistence of finite inertial effects.

1. Introduction

The problem of particle motion in rapidly rotating low-viscosity fluids was first considered by Proudman (1916) and Taylor (1917). When inertial and viscous forces are negligible within a rapidly rotating flow, the fluid motion is governed by a 'geostrophic' balance between Coriolis forces and pressure gradients. The Taylor–Proudman theorem requires that all fluid motions in a geostrophically balanced incompressible flow be independent of the spatial coordinate that varies in a direction parallel to the axis of rotation. Consequently, when a rigid axisymmetric body translates slowly on-axis through a low-viscosity fluid rotating rapidly about a vertical axis, a vertical column of fluid accompanies the body. The two-dimensional constraint imposed by the fluid's rotation may be relaxed by either inertial or viscous effects.

In early studies of axial particle motion in rotating fluids, inertial effects were

† Present address: Department of Applied Mathematics and Theoretical Physics, Silver Street, Cambridge, CB4 5HT, UK.

introduced through considering the unsteady geostrophic equations (Grace 1926). Stewartson (1952, 1953, 1958) considered the time-dependent problem of an impulsively started rigid body translating through an inviscid fluid, and thus deduced the steady asymptotic behaviour of the flow and the hydrodynamic force on the particle at long times. More recently, solutions have been sought to the steady viscous equations of motion in which all inertial terms are neglected. This approach was introduced by Morrison & Morgan (1956), and will be adopted in the theoretical analysis presented herein.

In the absence of inertial effects, the Taylor column which circumscribes a body rising on-axis has a vertical extent determined by the fluid viscosity. In the case of a buoyant particle rising on-axis through a sufficiently shallow horizontal fluid layer, the Taylor column will span the entire fluid depth, and the body cannot rise unless the Taylor–Proudman constraint is released. The body is able to rise only by way of small-scale viscous boundary layer motions which arise on the container and body surfaces and transport fluid from the fore to the aft regions of the Taylor column. In the case of a particle rising axially through an unbounded fluid, the two-dimensional constraint imposed by the fluid's rotation is once again released through viscous effects, which permit large-scale streaming past the body in vertical boundary layers. Qualitative representations of the flow fields for the bounded and unbounded cases are illustrated in figure 1. Figures 2, 3 and 4 (plate 1) illustrate a number of flow features characteristic of axial drop motion in rapidly rotating fluids as revealed in our laboratory through the use of tracer particles. In particular, the columnar structure accompanying the drop motion is clearly evident. Further details are provided in §6.

A summary of the investigations most relevant to our study of axial particle motion in rapidly rotating fluids is presented in table 1. To date, research has focused primarily on rigid particle motion. Morrison & Morgan (1956) considered the steady motion of a rigid disk in an unbounded viscous fluid. The unbounded problem was generalized to the case of an arbitrarily shaped rigid axisymmetric particle by Moore & Saffman (1969). Hocking, Moore & Walton (1979) considered the case of a sphere translating in a rapidly rotating container in which the flow is only weakly affected by boundaries. The problem of particle translation along the length of a vertical Taylor column spanning the entire depth of a bounded horizontal fluid layer was first treated by Moore & Saffman (1968), who considered the rise of rigid axisymmetric bodies. The case of a buoyant bubble rising between rigid horizontal boundaries was treated by Bush, Stone & Bloxham (1992), who deduced analytical solutions for both the bubble shape and rise speed. In this paper, we generalize previous studies of steady axial particle motion in low-viscosity fluids through calculating the shape and rise speed of a deformable drop of arbitrary viscosity.

Since the seminal experiments of Taylor (1921, 1922, 1923), a number of experimental investigations of axial particle motion in rapidly rotating fluids have been undertaken; however, the majority have been concerned with the effects of inertia on the particle and fluid motion (e.g. Long 1953; Pritchard 1969). The experiments of primary relevance to our study are those of Maxworthy (1968, 1970), who studied rigid particle motion in both the bounded and unbounded geometries. Maxworthy (1968) first considered the axial motion of rigid spheres in the bounded geometry, and demonstrated that the theoretical limit in which inertial effects may be safely neglected is not easily realized in the laboratory. While the observed rise speeds largely confirmed the theoretical predictions of Moore & Saffman (1968), they were typically larger than those predicted theoretically owing to inertial relaxation of the Taylor–Proudman constraint of two-dimensionality. Maxworthy (1970) also characterized particle

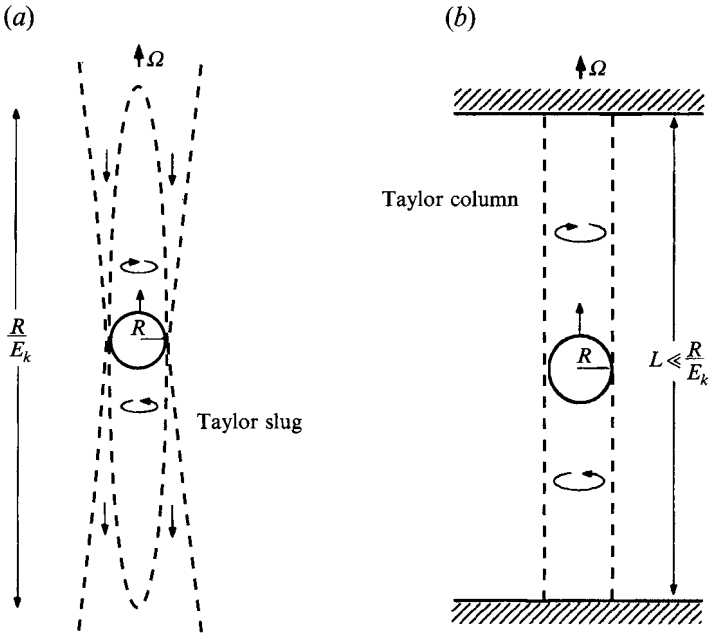

FIGURE 1. Schematic illustrations of the flow induced by the axial translation of buoyant particles through rapidly rotating fluids in (*a*) unbounded and (*b*) bounded geometries. Swirling motions of opposite sense are induced up- and downstream of the particle by the axial translation.

motion in the unbounded flow geometry, and observed steady rise speeds that were typically a factor $\pi/2$ smaller than those predicted theoretically by Moore & Saffman (1969).

Treatment of the deformable viscous drop problem entails consideration of the drop shape and internal flow. A buoyant drop is centrifugally stable on-axis and thus assumes the form of an axisymmetric body of revolution. In the rapid rotation limit, the dominant pressure in the problem is centrifugal; consequently, at leading order the drop shape is set by a balance between centrifugal and interfacial tension forces, and corresponds to the prolate ellipsoidal shape (Vonnegut 1942; Rosenthal 1962) which would arise in the absence of drop translation. The internal and external flows couple through a boundary layer on the drop's surface. In the bounded problem, the rise speed depends explicitly on the details of this boundary layer. Conversely, in the unbounded problem, a first approximation to the rise speed depends only on the equatorial radius of the drop, which in turn sets the cross-sectional radius of the Taylor column.

In the bounded geometry, vortex compression and stretching in the boundary layers, respectively, up- and downstream of the drop give rise to negative and positive relative vorticity, and thus large swirling motions of opposite sense in the fore and aft regions of the Taylor column. Ekman suction on the upstream drop and container surfaces and Ekman pumping on the downstream surfaces transport fluid from the fore to the aft regions of the Taylor column. In the case of rigid container boundaries (as illustrated in figure 6), the circuit of fluid transport from the upper to the lower container boundaries is completed by viscous internal boundary layers termed Stewartson layers (Greenspan 1968; Moore & Saffman 1969), which define the vertical walls of the Taylor column. In the case of free-slip (i.e. zero shear stress) container boundaries, Ekman transport occurs exclusively over the drop surface, and the drop rises only by virtue of its finite viscosity.

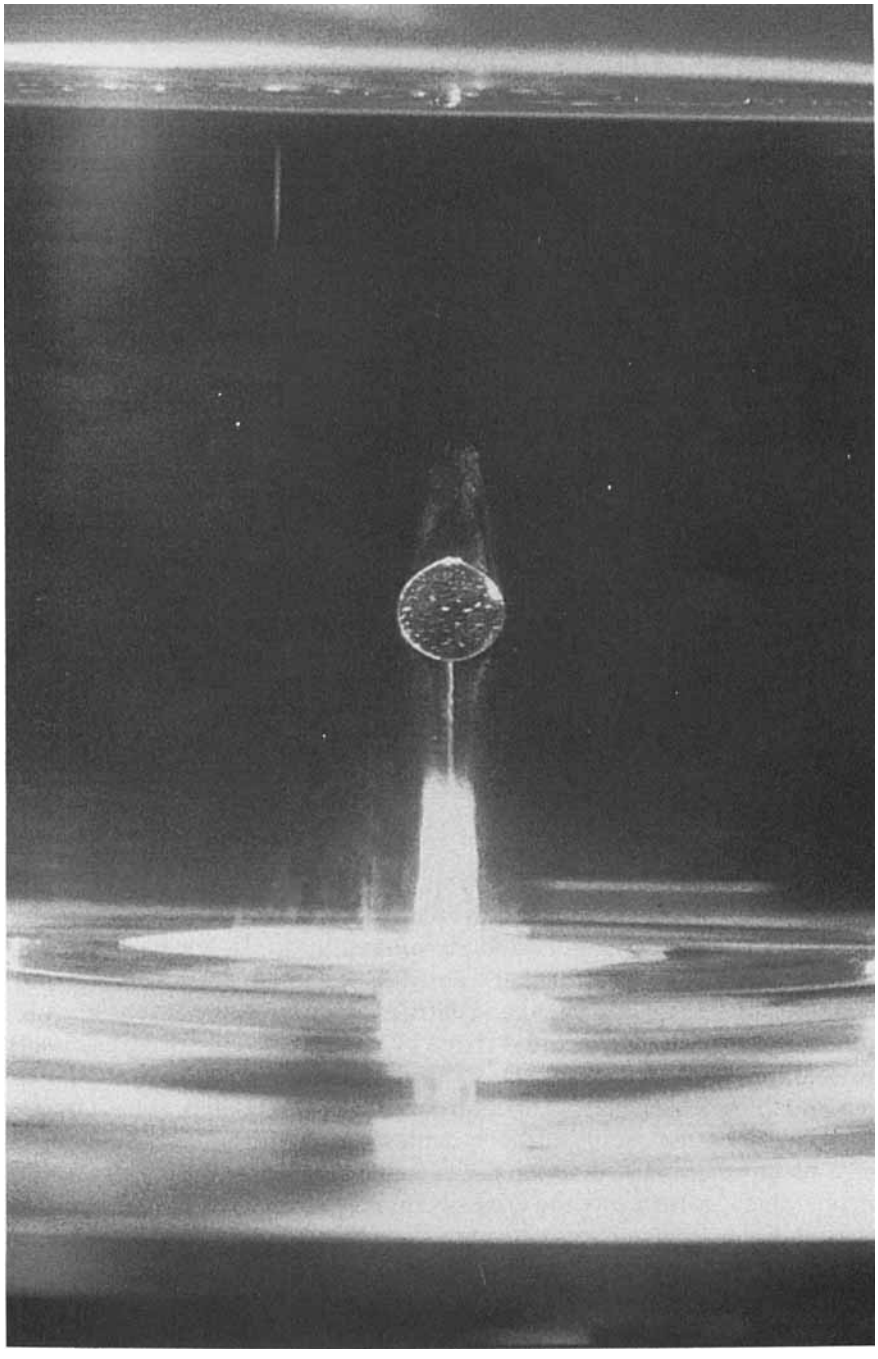

FIGURE 2. Drop of silicone fluid of radius 1.8 cm rising through water rotating at 56 r.p.m. Tracer particles illuminate the external Taylor column and the internal circulation.

The nature of the internal circulation depends critically on the viscosity of the drop. When the drop viscosity is sufficiently small, a geostrophic flow prevails inside the drop, and the boundary layer at the drop surface assumes the form of a double Ekman layer (Berman, Bradford & Lundgren 1978; Baker & Israeli 1981). The drop in this

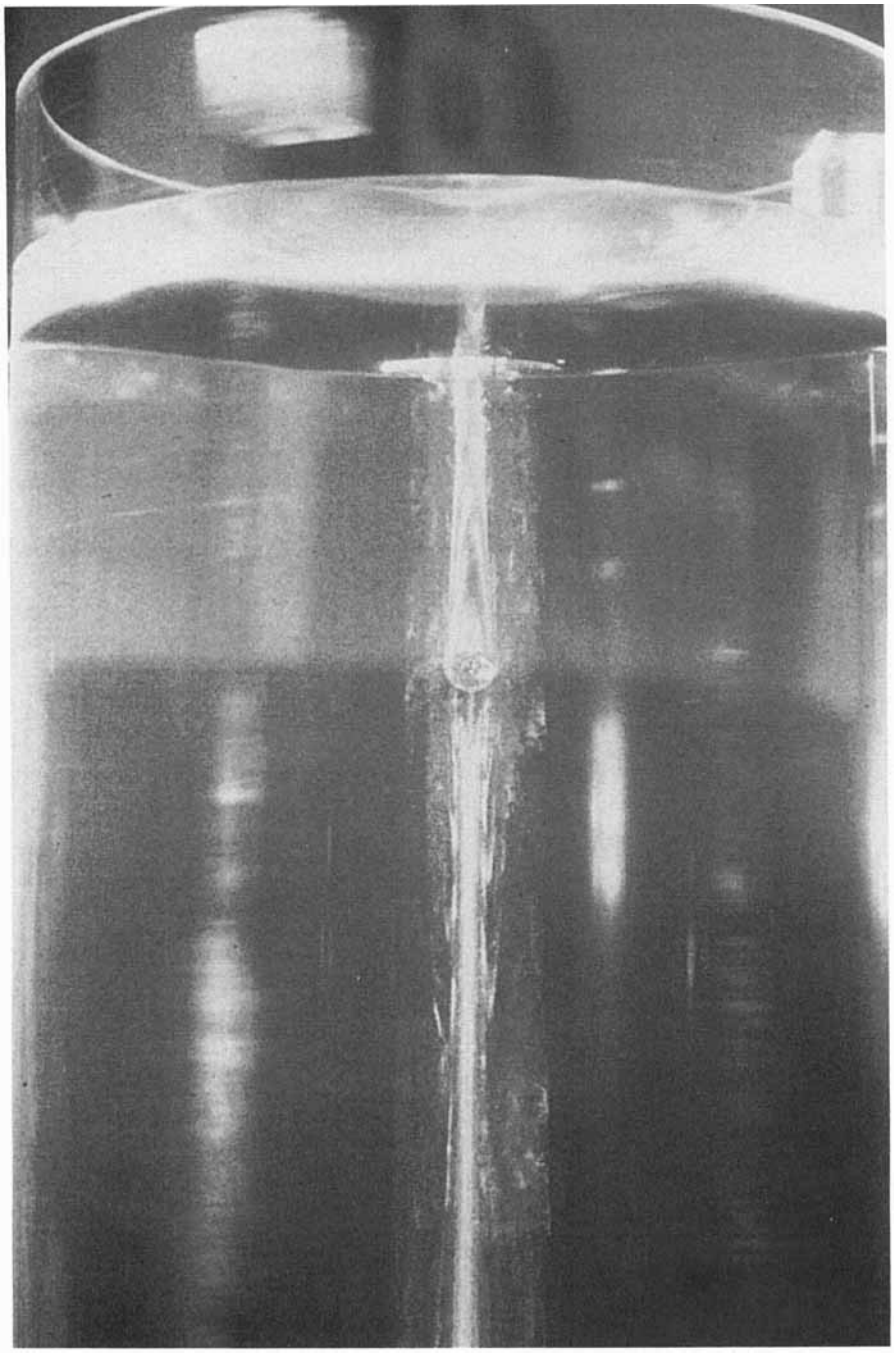

FIGURE 3. A drop of silicone fluid of radius 0.5 cm rising beneath a free surface. The rotation speed is 56 r.p.m. and the suspending fluid is water. The Taylor column extends to the forward boundary which thus has a pronounced influence on the rise speed.

case will henceforth be referred to as 'geostrophic'. In the case of a drop of sufficiently high viscosity, the internal motion may be described as a Stokes flow forced by Ekman stresses on the drop surface. The drop in this case will henceforth be referred to as a 'Stokes' drop.

	Rigid boundaries	Free-slip boundaries	Unbounded
Rigid particle	Moore & Saffman (1968) Hocking *et al.* (1979) Maxworthy (1968) (E)	Moore & Saffman (1968) Maxworthy (1968) (E)	Morrison & Morgan (1956) Moore & Saffman (1969) Maxworthy (1970) (E)
Viscous drop	Present work	Present work	Present work
Bubble	Bush *et al.* (1992)	Moore & Saffman (1968)	Present work

TABLE 1. An overview of theoretical and experimental (E) studies of slow steady on-axis particle motion in rapidly rotating low-viscosity fluids

We consider the steady motion of a deformable viscous drop bound by surface tension and rising on-axis in both the bounded and unbounded geometries, and give particular attention to the bounded problem. In §2, we describe in detail the form of the flow induced by the rising drop, and delineate the parameter regime to be considered in the theoretical analysis. The governing equations are presented in §2.1. Details of the drop shape calculation closely follow Bush *et al.* (1992) and are presented in §2.2. In §2.3, we first deduce an estimate for the rise speed in the bounded geometry by way of simple scaling analyses, and proceed by outlining the formal solution method. In §3, we obtain detailed solutions for the flow field induced by a geostrophic drop, and compute the drop's steady rise speed for a variety of boundary conditions. The case of a Stokes drop rising in the bounded geometry is considered in §4, where we demonstrate that the internal circulation is qualitatively different from that in the geostrophic drop. In §5, we briefly consider the case of a drop of arbitrary viscosity rising on-axis in the unbounded geometry. Finally, we describe a complementary experimental study of axial drop motion in bounded rotating fluids in §6.

2. Physical picture

Consider an incompressible fluid of density ρ and kinematic viscosity ν rotating about a vertical axis with constant angular velocity $\boldsymbol{\Omega}$ in the presence of a vertical gravitational field $\boldsymbol{g}$. The solid-body rotation of the fluid is disrupted by the slow steady on-axis rise at speed U of a buoyant drop of volume V, kinematic viscosity $\hat{\nu}$, and density $\hat{\rho} = \rho - \Delta\rho$. The drop surface is characterized by a constant interfacial tension σ. We introduce a cylindrical coordinate system (r, ϕ, z) with origin at the drop's centre-of-mass and with the z-axis vertical, so that $\boldsymbol{\Omega} = \Omega\,\hat{\boldsymbol{z}}$ and $\boldsymbol{g} = -g\hat{\boldsymbol{z}}$ (see figure 5). Henceforth, the superscripts '+' and '−' denote variables in the upstream ($z > 0$) and downstream ($z < 0$) regions of the fluid, respectively. The drop is assumed to be axisymmetric, with a steady shape specified by $z = f^{\pm}(r)$ for $r < R$, where R is the drop's 'equatorial' (maximum) radius. The detailed shape calculation which justifies this assumption is presented in §2.2.

2.1. *Governing equations*

In the rotating frame, the Navier–Stokes equations assume the form

$$\frac{\partial \boldsymbol{v}}{\partial t} + \boldsymbol{v}\cdot\nabla\boldsymbol{v} + 2\boldsymbol{\Omega}\wedge\boldsymbol{v} = -\frac{1}{\rho}\nabla p_d + \nu\nabla^2\boldsymbol{v}, \quad \nabla\cdot\boldsymbol{v} = 0, \tag{1}$$

where $\boldsymbol{v}(\boldsymbol{r}) = (u, v, w)$ is the fluid velocity relative to the rotating frame. The dynamic pressure p_d is related to the actual fluid pressure p by

$$p_d = p + \rho g z - \tfrac{1}{2}\rho\Omega^2 r^2. \tag{2}$$

FIGURE 4. A dyed silicone drop of radius 2 cm rising through water rotating at 56 r.p.m. The aspherical prolate distortion is associated with the small air bubbles, visible at the nose of the drop, which generally accompanied the injection of the tracer particles (see figure 2 also).

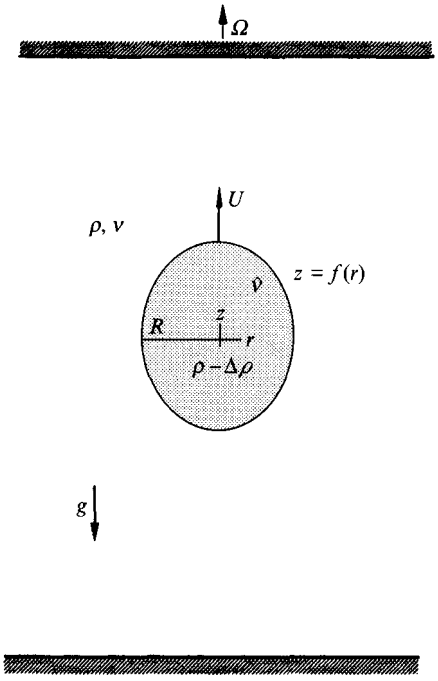

FIGURE 5. A drop rising on-axis between rigid horizontal boundaries.

We consider situations where the bulk external fluid motion is geostrophic, so that Coriolis forces are balanced by pressure gradients and the drop is circumscribed by a Taylor column. The translation of the drop produces swirling motions within the Taylor column of characteristic magnitude U_s and associated dynamic pressure variations of magnitude $\rho\Omega U_s R$. Choosing length, velocity, time, and pressure scales of, respectively, R, U_s, R/U_s and $\rho\Omega U_s R$ yields the dimensionless momentum equation

$$\mathscr{R}_o^s\left(\frac{\partial \boldsymbol{v}}{\partial t}+\boldsymbol{v}\cdot\boldsymbol{\nabla}\boldsymbol{v}\right)+2\hat{\boldsymbol{z}}\wedge\boldsymbol{v}=-\boldsymbol{\nabla}p_d+E_k\nabla^2\boldsymbol{v}. \tag{3}$$

The swirl Rossby number, $\mathscr{R}_o^s = U_s/R\Omega$, characterizes the relative importance of inertial to Coriolis forces, while the Ekman number, $E_k = \nu/\Omega R^2$, that of viscous to Coriolis forces. We consider the limit where the drop's steady rise speed U is sufficiently slow and the rotation rate of the fluid Ω sufficiently large that $\mathscr{R}_o^s \ll 1$ and $E_k \ll 1$, so that inertial and viscous effects may be ignored within the bulk of the external fluid, whose motion is governed by the geostrophic equation

$$2\hat{\boldsymbol{z}}\wedge\boldsymbol{v}=-\boldsymbol{\nabla}p_d. \tag{4}$$

Within the Taylor column, radial pressure gradients are balanced by Coriolis forces associated with the swirling motions: $2\rho\Omega v(r) = \mathrm{d}p/\mathrm{d}r$. Taking the curl of (4) yields the familiar Taylor–Proudman constraint of two-dimensionality: $\partial v/\partial z = 0$. The rising drop is circumscribed by a vertical Taylor column or 'slug' whose length is of order R/E_k in an unbounded fluid (Moore & Saffman 1969). In an experimental investigation of the unbounded problem, Maxworthy (1970) observed that the Taylor slug accompanying a rising particle is typically $O(0.1\ R/E_k)$.

In our analysis, which follows that of Moore & Saffman (1968), inertial effects are assumed to be negligible throughout the fluid, and viscous effects important only in

thin Ekman layers on the drop and container boundaries and in the Stewartson layers which define the walls of the Taylor column. The Ekman layers have characteristic thickness $\delta = (\nu/\Omega)^{1/2}$ and so are thin, $O(E_k^{1/2})$, relative to the drop's equatorial radius.

The flow inside the drop may be likewise described; however, as we are to consider the limits of both high and low internal viscosity, we allow some freedom in the choice of characteristic velocities and pressures for the internal flow. We denote inner variables with carats, and write

$$\hat{\mathscr{R}}_o\left(\frac{\partial \hat{\boldsymbol{v}}}{\partial t}+\hat{\boldsymbol{v}}\cdot\boldsymbol{\nabla}\hat{\boldsymbol{v}}\right)+2\hat{\boldsymbol{z}}\wedge\hat{\boldsymbol{v}}=-\frac{\hat{P}_c}{\hat{\rho}\Omega\hat{U}R}\boldsymbol{\nabla}\hat{p}_d+\hat{E}_k\nabla^2\hat{\boldsymbol{v}},\quad \boldsymbol{\nabla}\cdot\boldsymbol{v}=0, \tag{5}$$

where $\hat{P}_c$ and $\hat{U}$ are characteristic internal pressures and velocities, and $\hat{\mathscr{R}}_o = \hat{U}/R\Omega$ and $\hat{E}_k$ are the internal Rossby and Ekman numbers. In the limit $(\hat{\mathscr{R}}_o, \hat{E}_k) \ll 1$, we choose $\hat{U} = U_s$, so that the appropriate internal pressure scale is $\hat{P}_c = \hat{\rho}\Omega U_s R$, and a geostrophic balance exists within the drop:

$$2\hat{\boldsymbol{z}}\wedge\hat{\boldsymbol{v}}=-\boldsymbol{\nabla}\hat{p}_d. \tag{6}$$

In compliance with the Taylor–Proudman theorem, the bulk internal motion must correspond to a z-independent swirling motion. Viscous effects are dynamically important only within the internal boundary layer (of characteristic thickness $\hat{\delta} = (\hat{\nu}/\Omega)^{1/2}$) required to match the velocities and balance the tangential stresses across the drop surface.

In the limit of a high-viscosity drop ($\hat{R}e = \hat{U}R/\hat{\nu} \ll 1$, $\hat{E}_k \gg 1$), treated in detail in §4, the internal flow is characterized by a velocity scale $\hat{U} = U_s/(\lambda E_k^{1/2})$, and a viscous pressure scale $\hat{P}_c = \hat{\mu}\hat{U}/R$, where μ and $\hat{\mu} = \lambda\mu$ denote the viscosities of the external and internal fluids. In this limit, the equations (5) governing the internal flow reduce to Stokes equations:

$$-\boldsymbol{\nabla}\hat{p}_d+\nabla^2\hat{\boldsymbol{v}}=0,\quad \boldsymbol{\nabla}\cdot\hat{\boldsymbol{v}}=0. \tag{7}$$

For such a high-viscosity drop ($\lambda \gg 1$), the internal and external flows uncouple to leading order: the external motion corresponds to flow past a rigid particle, and the internal motion to a Stokes flow driven by tangential stresses applied at the drop surface.

2.2. *Drop shape calculation*

In this section we consider the shape of a fluid drop rising along the axis of rotation. The normal stress jump across the interface is balanced by the curvature force associated with the interfacial tension σ. Using stress tensors defined in terms of the dynamic pressure p_d, e.g. $\boldsymbol{T}_d = -p_d\boldsymbol{I}+2\mu\boldsymbol{E}$, we write the dimensional normal stress balance as

$$(\hat{p}_0-p_0)-\Delta\rho\tfrac{1}{2}\Omega^2 r^2+\Delta\rho g z+\boldsymbol{n}\cdot(\boldsymbol{n}\cdot\boldsymbol{T}_d-\boldsymbol{n}\cdot\hat{\boldsymbol{T}}_d)=\sigma\boldsymbol{\nabla}_s\cdot\boldsymbol{n}, \tag{8}$$

where $\hat{p}_0$ and p_0 are constant reference pressures inside and outside the drop, and $\boldsymbol{n}$ is the unit normal directed outward from the drop. The relative magnitudes of the various components of the normal stress at the drop surface are given by

$$\frac{\text{geostrophic}}{\text{centrifugal}}\approx\frac{\rho\Omega R U_s}{\Delta\rho\,\Omega^2 R^2}\approx\mathscr{R}_o^s\frac{\rho}{\Delta\rho}, \tag{9}$$

$$\frac{\text{hydrostatic}}{\text{centrifugal}}\approx\frac{g}{R\Omega^2}\approx\mathscr{R}_o^s\frac{\rho}{\Delta\rho}, \tag{10}$$

$$\frac{\text{viscous}}{\text{centrifugal}}\approx\frac{\mu U_s/\delta}{\Delta\rho\,\Omega^2 R^2}\approx\mathscr{R}_o^s E_k^{1/2}\frac{\rho}{\Delta\rho}, \tag{11}$$

where a typical rise speed in the bounded geometry (e.g. U_0 defined in (13)) has been used to simplify (10). In the dynamic regime of interest ($E_k, \mathscr{R}_o^s \ll 1$), and for $\Delta\rho/\rho \approx O(1)$, the geostrophic, hydrostatic, and viscous contributions to the normal stress balance are negligible. At leading order, the dimensionless normal stress balance (8) thus assumes the form describing the shape of a stationary drop in a rotating fluid,

$$P + 4\Sigma r^2 = \nabla_s \cdot \boldsymbol{n}, \tag{12}$$

where $\Sigma = -\Omega^2 R^3 \Delta\rho/8\sigma$ is the rotational Bond number and P is a constant. The drop shape is determined by a balance between the centrifugal force, which acts to drive the lighter drop fluid along the axis of rotation, and the force due to interfacial tension and curvature, which tends to maintain the sphericity of the drop. For the case of a buoyant drop, $\Sigma < 0$, the shape is prolate ellipsoidal, with an ellipticity determined by Σ (Rosenthal 1962). These prolate figures of revolution have been demonstrated to be stable to small disturbances (Ross 1968*a*, *b*).

The contributions to the normal stress balance from the hydrostatic and geostrophic components are negligible to leading order, so that the drop assumes a fore–aft axisymmetric shape. This symmetry will simplify the calculation of the drop's rise speed in §3. Detailed knowledge of the flow induced by the drop translation, as will be determined in §3, makes it possible to infer the precise form of the dynamic pressure in the external fluid and so to determine the small corrections to the drop shape necessitated by terms neglected in (12). In Appendix A, we consider the special case of a spherical bubble, and illustrate the fore–aft asymmetric distortion associated with the hydrostatic and geostrophic pressure fields. A perturbation analysis demonstrates that the combined effect of the hydrostatic and geostrophic pressures is to distort a spherical bubble into a bullet shape, which is slightly flattened at the back surface and elongated at the front.

2.3. *Rise speed calculation*

Since the swirling motions induced by the drop motion are of opposite sense in the fore and aft regions of the Taylor column, the concomitant geostrophic pressure defects are of opposite sign; in particular, geostrophic high- and low-pressure regions exist, respectively, up- and downstream of the drop. The pressure jump across the bubble surface results in a hydrodynamic force, or drag, of characteristic magnitude $\pi\rho R^3 \Omega U_s$. In the case of a bounded horizontal plane layer, swirling motions, $U_s = O(U/E_k^{1/2})$, are generated within the Taylor column by vortex stretching and compression in Ekman layers on the drop and container surfaces. Equating the geostrophic drag, $\pi\rho R^2 \Omega U/E_k^{1/2}$, with the buoyancy force, $g\Delta\rho V$, yields a characteristic rise speed U_0 given by

$$U_0 = \frac{V}{\pi R^4} \frac{\Delta\rho}{\rho} \frac{g}{\Omega} \left(\frac{\nu}{\Omega}\right)^{1/2}. \tag{13}$$

While U_0 has been deduced from a simple scaling analysis, it corresponds precisely to the rise speed of an inviscid drop between rigid horizontal boundaries (Bush *et al.* 1992). The fluid viscosity acts to release the constraint imposed by the fluid's rotation through generation of Ekman transport from the fore to the aft column regions; consequently, the rise speed increases with fluid viscosity as $\nu^{1/2}$ and decreases with rotation rate as $\Omega^{-3/2}$.

In the case of the 'geostrophic' drop, the tangential stress balance at the drop interface, namely, $\mu U_s/\delta \approx \hat{\mu}\hat{U}/\hat{\delta}$, indicates the importance of the parameter $\beta = \hat{\rho}/\rho(\hat{\nu}/\nu)^{1/2}$, through which the drop's fluid properties enter the analysis. The rise

speed further depends on the form of the horizontal boundaries of the fluid domain. We characterize the nature of stress transmission at the top and bottom container boundaries with the respective parameters c_t and c_b, which assume the value 1 if the appropriate boundary is rigid, and 0 if it is a free-slip (or zero shear stress) surface. We thus write the general result for the rise speed of a drop between horizontal boundaries as

$$\frac{U}{U_0} = \mathscr{F}(\beta, \Sigma, c_t, c_b). \tag{14}$$

The principal contribution of this paper is the determination of the form of the function $\mathscr{F}$.

The rise speed of the drop is determined by balancing the buoyancy force with the drag exerted by the external fluid, which is calculated by integrating the viscous and pressure stresses over the drop surface. The magnitude of the viscous stress relative to the dynamic pressure contribution is given by $\mu U_s/\delta/(\rho\Omega U_s R) \approx E_k^{1/2}$, which is necessarily small in the parameter regime of interest. The drag D may thus be expressed in dimensionless terms, accurate to $O(E_k^{1/2})$, as

$$\frac{D}{\rho R^3 \Omega U_s} = \int_S p_d \, \boldsymbol{z}\cdot\boldsymbol{n} \, \mathrm{d}S = 2\pi \int_0^1 r[p_d^+(r, f^+(r)) - p_d^-(r, f^-(r))] \, \mathrm{d}r. \tag{15}$$

The drag may be written in terms of the geostrophic swirl velocities within the Taylor column by using the radial component of (4), which yields

$$\frac{D}{\pi\rho R^3 \Omega U_s} = 2\int_0^1 r^2[v^-(r) - v^+(r)] \, \mathrm{d}r. \tag{16}$$

In the bounded problem, the swirl velocities v are related to the rise speed U through Ekman compatibility conditions, which relate the secondary vertical fluxes into the boundary layers on the container and drop boundaries to the primary swirling motions within the Taylor column. The Ekman compatibility conditions to be applied at the container boundaries are standard (Greenspan 1968). The determination of the appropriate Ekman compatibility conditions at the drop surface requires consideration of the internal drop dynamics.

3. Low-viscosity drops in bounded geometries

In the limit $(\hat{\mathscr{R}}_o, \hat{E}_k) \ll 1$, a geostrophic balance exists within the drop. The bulk internal motion must correspond to a z-independent swirling motion $\hat{v}(r)$, and the drop surface corresponds to a curved double Ekman layer. The form of the curved double Ekman layer and the associated Ekman compatibility conditions have been described by Berman *et al.* (1978), and are briefly summarized in Appendix B. We now apply the appropriate Ekman compatibility conditions, equation (B 2) for a stationary horizontal boundary and (B 4) for a double Ekman layer. The Ekman compatibility conditions take the explicit form:

upper container surface

$$w^+(r) = -c_t \frac{E_k^{1/2}}{2r} \frac{\mathrm{d}}{\mathrm{d}r}(rv^+(r)); \tag{17}$$

upper drop surface

$$\hat{w}(r) - E_k^{1/2} = \frac{\rho}{\hat{\rho}}(w^+(r) - E_k^{1/2}), \tag{18}$$

$$w^+(r) - E_k^{1/2} = \frac{\beta}{1+\beta}\frac{E_k^{1/2}}{2r}\frac{\mathrm{d}}{\mathrm{d}r}(r(v^+(r) - \hat{v}(r))[1+f'^2]^{1/4}); \tag{19}$$

lower drop surface

$$\hat{w}(r) - E_k^{1/2} = \frac{\rho}{\hat{\rho}}(w^-(r) - E_k^{1/2}), \tag{20}$$

$$w^-(r) - E_k^{1/2} = -\frac{\beta}{1+\beta}\frac{E_k^{1/2}}{2r}\frac{\mathrm{d}}{\mathrm{d}r}(r(v^-(r) - \hat{v}(r))[1+f'^2]^{1/4}); \tag{21}$$

lower container surface

$$w^-(r) = c_b\frac{E_k^{1/2}}{2r}\frac{\mathrm{d}}{\mathrm{d}r}(rv^-(r)). \tag{22}$$

All velocities in equations (17)–(22) have been non-dimensionalized with respect to the characteristic swirl, $U/E_k^{1/2}$, and the vertical velocities are measured relative to the stationary container boundaries. The constant term $E_k^{1/2}$ appearing in (18)–(21) thus indicates the uniform translation of the drop surface.

Equations (18)–(21) demonstrate that the swirl velocity within the drop is the average of the swirls above and below the drop,

$$\hat{v}(r) = \tfrac{1}{2}(v^+(r) + v^-(r)), \tag{23}$$

and also that $w^+(r) = w^-(r)$. Subtracting (17) from (19) and using (23) yields a relation between the dimensionless rise speed and the swirl velocities up- and downstream of the drop

$$1 = -\frac{1}{2r}\frac{\mathrm{d}}{\mathrm{d}r}\left(c_t rv^+(r) + \frac{\beta}{1+\beta}\frac{r}{2}(v^+(r) - v^-(r))[1+f'^2]^{1/4}\right). \tag{24}$$

Similarly, (21) and (22) yield

$$1 = \frac{1}{2r}\frac{\mathrm{d}}{\mathrm{d}r}\left(c_b rv^-(r) + \frac{\beta}{1+\beta}\frac{r}{2}(v^-(r) - v^+(r))[1+f'^2]^{1/4}\right). \tag{25}$$

Comparison of (24) and (25) reveals that the swirl velocities above the below the drop are related by

$$c_b v^-(r) = -c_t v^+(r). \tag{26}$$

Substituting (26) into (24) and integrating radially from 0 to r yields the form of the upstream swirl velocity:

$$v^+(r) = -\frac{r}{c_t + \frac{1}{2}(1 + c_t/c_b)[1+f'^2]^{1/4}\beta/(1+\beta)}. \tag{27}$$

Equations (26) and (27) may be substituted directly into (16) in order to deduce the dimensional drag D on the drop:

$$\frac{D}{\pi\rho R^3 \Omega U/E_k^{1/2}} = 2\int_0^1 \frac{r^3(1 + c_t/c_b)\,\mathrm{d}r}{c_t + \frac{1}{2}(1 + c_t/c_b)[1+f'^2]^{1/4}\beta/(1+\beta)}, \tag{28}$$

which can be integrated provided the detailed drop shape $f(r)$ is known.

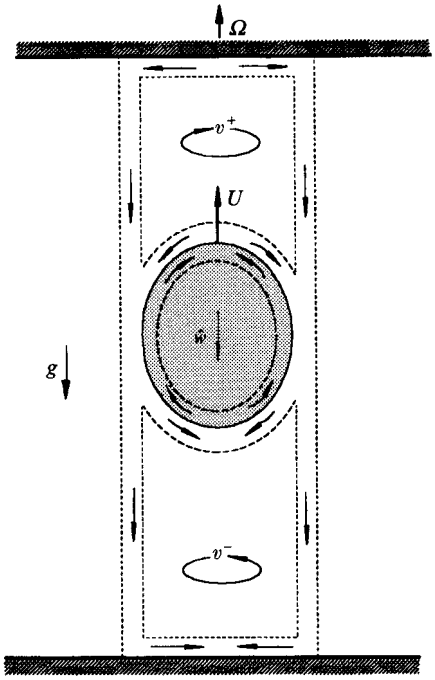

FIGURE 6. A schematic illustration of the flow induced by a low-viscosity ('geostrophic') drop rising between rigid horizontal boundaries. The drop interface is characterized by a double Ekman layer, and the internal flow by a weak downward flow (relative to the drop surface).

Equating the drag D with the buoyancy force, $Vg\Delta\rho$, yields the steady rise speed:

$$\frac{U}{U_0} = 2\left(\int_0^1 \frac{r^3(1+c_t/c_b)\,\mathrm{d}r}{c_t+\frac{1}{2}(1+c_t/c_b)[1+f'^2]^{1/4}\beta/(1+\beta)}\right)^{-1}, \tag{29}$$

where U_0 is the rise speed of a bubble between rigid horizontal boundaries introduced in (13). The rise speed depends on both the fluid properties (which enter through the single parameter β) and the drop shape. Equations (17)–(22) also yield the form of the flow inside the drop. The swirl along the drop surface, denoted by v_{int}, is determined from a detailed analysis of the double Ekman layer (see Appendix B). We thus obtain

$$\hat{w}(r) - E_k^{1/2} = -\frac{\rho}{\hat{\rho}}\frac{\beta}{1+\beta}\frac{E_k^{1/2}}{2r}\frac{\mathrm{d}}{\mathrm{d}r}\left(\frac{r^3(1+c_t/c_b)}{c_t+\frac{1}{2}(1+c_t/c_b)[1+f'^2]^{1/4}\beta/(1+\beta)}\right), \tag{30}$$

$$v_{int}^{+}(r) = \frac{1}{1+\beta}v^{+}(r)\,(1+\tfrac{1}{2}\beta(1-c_t/c_b)), \tag{31}$$

$$v_{int}^{-}(r) = \frac{1}{1+\beta}v^{+}(r)\,(\tfrac{1}{2}\beta(1-c_t/c_b)-c_t/c_b)). \tag{32}$$

Note that $v^{+}(1) = 0$ according to (27) since $|f'(1)| \to \infty$; consequently, the surface velocity is continuous at the drop equator: $v_{int}^{+}(1) = v_{int}^{-}(1) = 0$.

3.1. *The effect of the container boundaries*

Rigid boundaries ($c_t = c_b = 1$): A qualitative representation of the flow induced by a low-viscosity drop rising between rigid boundaries is illustrated in figure 6. Ekman transport occurs over both the drop and container surfaces. Continuity requires that

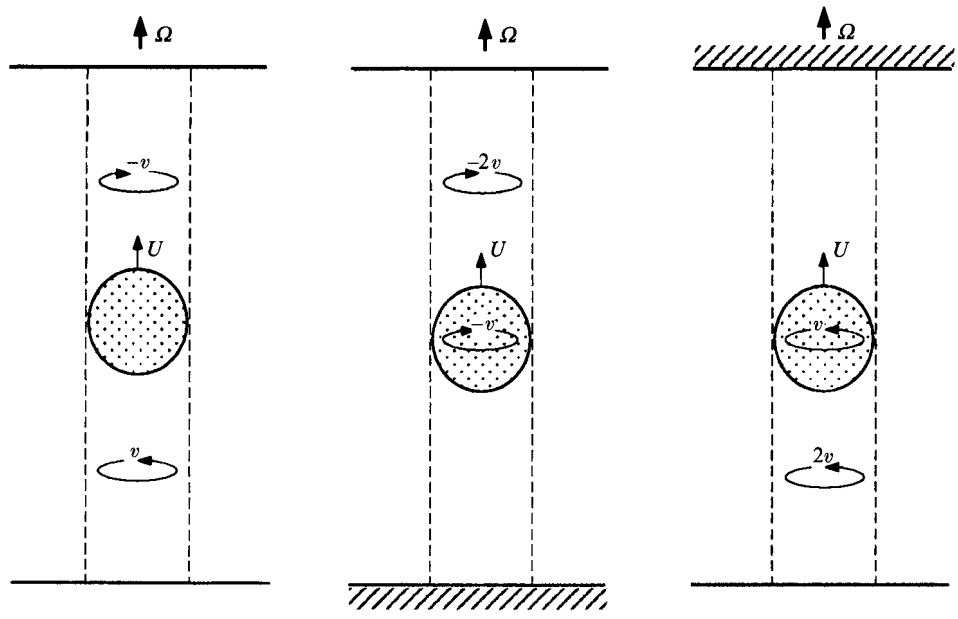

FIGURE 7. A schematic illustration of the flows induced by a geostrophic drop rising between different combinations of stress-free (unhatched) and rigid (hatched) boundaries. In each case, Ekman transport occurs exclusively over the drop surface, and the drops rise only by virtue of their finite viscosity. While the flows are qualitatively different, the drop rise speeds are identical.

the transport over the container boundaries be completed through vertical transport in the Stewartson layers which define the walls of the Taylor column. These internal viscous boundary layers assume the classic sandwich structure, with an inner layer of $O(E_k^{1/4})$ thickness in which the vertical transport occurs, and outer layers of $O(E_k^{1/3})$ in which swirling motions are matched (Greenspan 1968; Moore & Saffman 1969). Swirling motions of equal magnitude and opposite sense arise in the fore and aft regions of the Taylor column; thus, according to (23), there is no geostrophic swirling motion within the drop:

$$v^+(r) = -v^-(r) = -\frac{r}{1+(1+f'^2)^{1/4}\beta/(1+\beta)}, \quad \hat{v}(r) = 0. \tag{33}$$

The top and bottom drop surfaces rotate in the same sense as the fluid in, respectively, the up- and downstream regions of the Taylor column, with magnitudes

$$v_{int}^+(r) = -v_{int}^-(r) = -\frac{\beta}{1+\beta}\frac{r}{1+(1+f'^2)^{1/4}\beta/(1+\beta)}. \tag{34}$$

The motions on the upper and lower interface correspond to swirling motions of opposite sense; consequently, the flow driven within the drop may be likened to that driven by counter-rotating spherical caps (Greenspan 1968). The internal flow is characterized by an order $E_k^{1/2}$ downward flow driven by Ekman pumping and suction on, respectively, the upper and lower inner drop surfaces:

$$\hat{w}(r) = -\frac{\rho}{\hat{\rho}}\frac{\beta}{1+\beta}\frac{E_k^{1/2}}{2r}\frac{\mathrm{d}}{\mathrm{d}r}\left(\frac{r^2}{1+(1+f'^2)^{1/4}\beta/(1+\beta)}\right). \tag{35}$$

The rise speed of a drop between rigid upper and lower boundaries, U_{rr}, depends on the drop's shape and the viscosity parameter β as

$$\frac{U_{rr}}{U_0} = 4\left(\int_0^1 \frac{r^3\,\mathrm{d}r}{1+(1+f'^2)^{1/4}\beta/(1+\beta)}\right)^{-1}. \tag{36}$$

In the limit of an inviscid drop, $\beta \to 0$, Ekman transport over the drop surface is precluded, the rise speed is a minimum, and (36) yields the rise speed of a bubble: $U = U_0$ (Bush *et al.* 1992). For a particular shape, the rise speed increases monotonically with β. In the $\beta \to \infty$ limit, the rise speed is a maximum, and the rigid particle result of Moore & Saffman (1968) obtains.

Free-slip boundaries ($c_t = c_b = 0$). Once again, symmetry in the boundary conditions ensures that the swirling motions up- and downstream of the drop be equal and opposite, and that there be no geostrophic swirl within the drop (see figure 7):

$$v^+(r) = -v^-(r) = -\frac{1+\beta}{\beta}\frac{r}{(1+f'^2)^{1/4}}, \quad \hat{v}(r) = 0. \tag{37}$$

Counter-rotating upper and lower drop surfaces once again generate a downward flow within the geostrophic drop interior of magnitude $\hat{w}(r) = (\rho/\hat{\rho})\,U_{ff}$, where the rise speed of a drop between free-slip boundaries, U_{ff}, is given by

$$\frac{U_{ff}}{U_0} = \frac{4\beta}{1+\beta}\left(\int_0^1 \frac{r^3\,\mathrm{d}r}{(1+f'^2)^{1/4}}\right)^{-1}. \tag{38}$$

In this case, no Ekman transport occurs over the container boundaries, and the drop rises only by virtue of its finite viscosity. Fluid is transported from the fore to the aft regions of the Taylor column exclusively through boundary layer transport over the drop surface, thereby obviating the need for vertical transport in the Stewartson layers. In the limit of an inviscid drop, $\beta \to 0$, Ekman transport from the fore to the aft regions of the Taylor column is precluded entirely, and the bubble cannot rise. This paradoxical result indicates the limitations of the geostrophic approximation in describing this flow situation. As first discussed by Moore & Saffman (1968), the precise manner in which the Taylor–Proudman theorem is relaxed in the limit $\beta = 0$ remains an open question.

Rigid lower and free-slip upper boundaries ($c_t = 0$, $c_b = 1$): The asymmetry in the boundary conditions generates an asymmetry in the flow field; in particular, there is a swirling motion above but not below the drop, and a non-zero geostrophic swirl arises within the bulk of the drop:

$$v^+(r) = 2\hat{v}(r) = -\frac{1+\beta}{\beta}\frac{r}{(1+f'^2)^{1/4}}, \quad v^-(r) = 0. \tag{39}$$

While the flow fields generated by drops rising between free-slip and mixed (free-slip upper and rigid lower) container boundaries are thus markedly different, as illustrated schematically in figure 7, the rise speeds are identical; consequently, the rise speed equation (38) applies also to the case of mixed boundaries. Moreover, the magnitude of the vertical velocity generated inside the drop is identical in the case of mixed and free boundaries.

Since the stress-free upper surface cannot support an Ekman layer, there is no Ekman suction on the upper container boundary, no vertical transport in the Stewartson layers, no Ekman pumping on the lower boundary, and no swirling motion

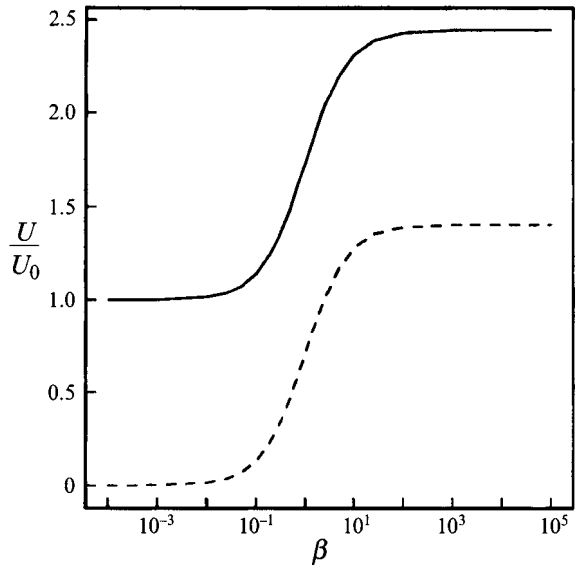

FIGURE 8. The rise speed of geostrophic spherical drops between rigid (solid curve) and stress-free (dashed curve) horizontal boundaries, as a function of the viscosity parameter $\beta = (\hat{\rho}/\rho)(\hat{\nu}/\nu)^{1/2}$. Rise speeds are normalized with respect to that of a spherical inviscid drop rising between rigid boundaries, U_0, as defined in (13).

downstream of the drop. As in the case of stress-free upper and lower boundaries, transport from the fore to the aft column regions is confined to the drop surface. Finally, since a free surface does not support an Ekman layer, the shape of the upper surface (provided it is axisymmetric) is dynamically unimportant; therefore, the rise speed result (38) applies equally well to the case of a drop rising on-axis beneath a free surface curved arbitrarily by centrifugal effects.

Likewise in the case of rigid upper and free-slip lower boundaries ($c_t = 1$, $c_b = 0$), swirling motions are confined to the Taylor column region adjacent to the free-slip surface (below the drop), Ekman transport is confined to the drop surface, and the drop rises with speed U_{ff}.

3.2. *Spherical drops: the effect of* β

When the internal motion may be described as geostrophic, we have demonstrated that the rise speed of a drop through a bounded fluid layer depends on its shape in addition to its physical properties, $\hat{\rho}$ and $\hat{\nu}$, which enter the analysis through the single parameter β. We proceed by illustrating the explicit dependence of rise speed on β by considering the case of spherical drops which arise naturally in the limit of large interfacial tension (small rotational Bond number). Figure 8 illustrates the dependence of rise speed on β for a spherical drop rising between rigid (upper curve) and stress-free (lower curve) container boundaries. For a particular value of β, the rise speed is always larger for the rigid than the free-slip boundary case owing to the additional Ekman transport over the container boundaries. In both cases, the rise speed is a minimum for the case of a bubble ($\beta = 0$) and a maximum for the case of a rigid sphere ($\beta \to \infty$). Between these two limits, the rise speed increases monotonically with β since increasing the drop viscosity serves to enhance the efficiency of Ekman transport over the drop surface, and so facilitates the rise of the drop.

As a caveat, we note that the results presented in figure 8 are based on the

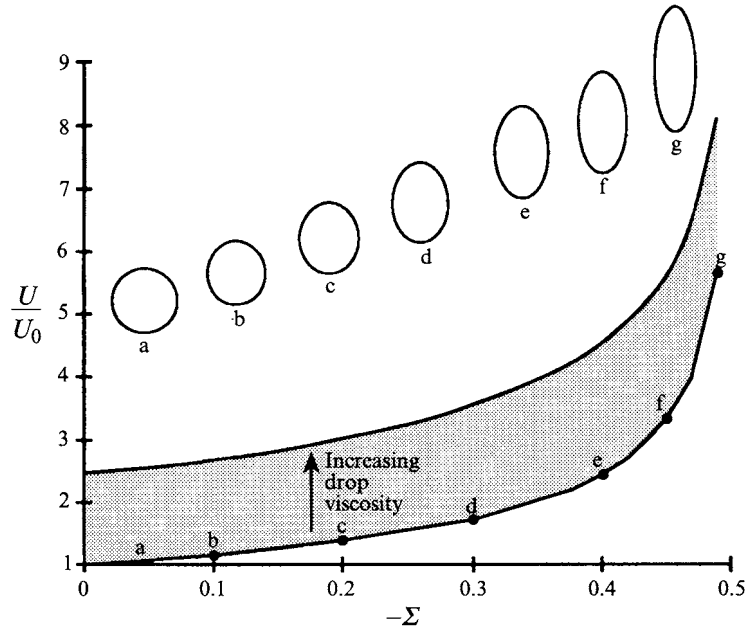

FIGURE 9. Rise speed and shape of a fluid drop bound by surface tension and rising on-axis between rigid horizontal boundaries, as a function of the rotational Bond number Σ. The lower curve represents the rise speed of an inviscid drop and the upper curve that of an identically shaped rigid body. The result (36) makes it possible to span the intermediate finite-β regime. Rise speeds are normalized with respect to that of a spherical inviscid drop and deformed shapes are scaled such that the volumes correspond to that of the undeformed spherical drop.

assumption that a geostrophic balance exists inside the drop, and so must eventually become invalid when the drop viscosity increases to a value such that $\hat{E}_k = O(1)$. Nonetheless, in the large-β limit, the geostrophic theory predicts that the swirling motion at the interface will come to rest, so that the external fluid effectively encounters a stationary rigid surface. It is thus that the theory based on the assumption of a geostrophic drop interior is capable of reproducing the rigid particle result of Moore & Saffman (1968). A consistent model of high-viscosity drop motion will be presented in §4.

3.3. *Coupling shape and rise speed analyses*

We have demonstrated that to leading order drops rising on axis assume a prolate ellipsoidal shape determined by the rotational Bond number Σ, and further that the drop's rise speed depends only on the drop shape $f(r)$ and the viscosity parameter β. For the bounded problem, we may thus uniquely deduce the drop's velocity as a function of two parameters Σ and β.

Figure 9 illustrates the shape and rise speed of a drop between rigid boundaries as a function of the rotational Bond number. The lower curve indicates the rise speed of a bubble ($\beta = 0$) which, according to (13), is independent of the bubble's detailed shape and depends only on its equatorial radius to the inverse fourth power. In the limit of large surface tension ($\Sigma \to 0$), the bubble is spherical, the equatorial radius a maximum, and the rise speed a minimum. As rotational effects become more important, and Σ decreases through the range $(0, -\frac{1}{2})$, the bubble becomes progressively more prolate, the equatorial radius decreases, and the rise speed increases accordingly. In the limit of $\Sigma \to -\frac{1}{2}$, the bubble tends toward a cylindrical thread; thus, according to our theory,

the rise speed increases without bound. In this limit, viscous effects are expected to dominate the external dynamics ($E_k > 1$), so that a geostrophic balance no longer adequately describes the external flow.

The upper curve in figure 9 indicates the rise speed of equivalently shaped rigid particles, which rise faster than bubbles due to additional Ekman transport over the rigid surface. Finally, the results of § 3.1 make it possible to fill in the intervening finite-β regime for drops of finite viscosity.

4. High-viscosity drops in bounded geometries

In the limit of a high-viscosity drop ($\hat{R}e \ll 1$, $\hat{E}_k \gg 1$), the equations governing the internal flow reduce to Stokes equations (7). The dimensional tangential stress balance at the drop surface indicates that $\hat{\mu}\hat{U}/R \approx \mu U_s/\delta$, where $\hat{U}$ and R denote characteristic length and velocity scales for the internal flow. The relative magnitudes of the velocities associated with the stress-driven internal flow and the external geostrophic flow are thus $\hat{U}/U_s = O(\lambda^{-1} E_k^{-1/2})$, where $\lambda = \hat{\mu}/\mu \gg 1$ denotes the viscosity ratio. Provided $\hat{\rho}/\rho = O(1)$, then $\hat{E}_k = (\lambda\rho/\hat{\rho})\,\mathrm{E_k} \gg 1$ implies that the viscously dominated internal motions are very slow relative to the geostrophic swirls: $\hat{U}/U_s = O(\lambda^{-1}\hat{E}_k^{-1/2}) \ll 1$.

We proceed by deducing the form of the flow associated with a high-viscosity drop rising along the length of a Taylor column. For simplicity, we consider the case of a spherical drop, and treat the problem in spherical polar coordinates $(\bar{r}, \theta, \phi)$. The preceding scaling analysis suggests the utility of a perturbation analysis appropriate for very slow internal flows. We expand the internal and external velocities, respectively, $\boldsymbol{v}(\boldsymbol{r})$ and $\hat{\boldsymbol{v}}(\boldsymbol{r})$, in powers of the small parameter $\epsilon = \lambda^{-1} E_k^{-1/2}$ which characterizes the magnitude of the slow internal motion:

$$\boldsymbol{v}(\boldsymbol{r}; E_k, \lambda) = \boldsymbol{v}_0(\boldsymbol{r}; E_k) + \epsilon \boldsymbol{v}_1(\boldsymbol{r}; E_k) + \ldots, \tag{40}$$

$$\hat{\boldsymbol{v}}(\boldsymbol{r}; E_k, \lambda) = \epsilon \hat{\boldsymbol{v}}_0(\boldsymbol{r}; E_k) + \ldots. \tag{41}$$

To zeroth order ($\epsilon = 0$), the external flow $\boldsymbol{v}_0(\boldsymbol{r}; E_k)$ corresponds to that past a rigid sphere, specifically a geostrophic swirl with a narrow viscous boundary layer. The surface stresses associated with the boundary layers on the drop generate an $O(\epsilon)$ internal flow, $\hat{\boldsymbol{v}}_0(\boldsymbol{r})$, which in turn alters the boundary conditions on the external flow, and so necessitates an $O(\epsilon)$ adjustment, $\boldsymbol{v}_1(\boldsymbol{r})$, to the external flow. In particular, the swirling velocities within the Taylor column increase by an amount of $O(\epsilon)$, and the Ekman transport over the drop surface decreases accordingly. The drag correction associated with the slow internal motion and the associated change in the geostrophic pressure field is thus $O(\epsilon)$; however, since $\epsilon \ll E_k^{1/2}$, this correction is negligible compared to the $O(E_k^{1/2})$ viscous drag neglected in the boundary layer approximation applied in the derivation of (16). Consequently, the perturbation analysis will not serve to illustrate in a self-consistent fashion the dependence of rise speed on drop viscosity for a high-viscosity drop. However, the analysis does yield the approximate form of the flow induced inside the drop.

The form of the Ekman layer flow, $\boldsymbol{v}_0(\boldsymbol{r})$, on a rigid sphere is given by

$$u_{\bar{\theta}}^{\pm}(\bar{r}, \theta) = -v^{\pm}(r) \exp\left[-\frac{(\bar{r}-1)}{E_k^{1/2}}(\pm\cos\theta)^{1/2}\right] \sin\left[\frac{(\bar{r}-1)}{E_k^{1/2}}(\pm\cos\theta)^{1/2}\right], \tag{42}$$

$$u_{\bar{\phi}}^{\pm}(\bar{r}, \theta) = v^{\pm}(r)\left(1 - \exp\left[-\frac{(\bar{r}-1)}{E_k^{1/2}}(\pm\cos\theta)^{1/2}\right] \cos\left[\frac{(\bar{r}-1)}{E_k^{1/2}}(\pm\cos\theta)^{1/2}\right]\right), \tag{43}$$

where $r = \bar{r}\sin\theta$ is the cylindrical radial coordinate, and $v^{\pm}(r)$ denote the external geostrophic swirling motions. This solution breaks down in the neighbourhood of the drop equator. For the case of a rigid sphere rising between rigid horizontal boundaries, the dimensional geostrophic swirl velocities in the over- and underlying Taylor column may be deduced directly from (33) by taking the limit $\beta \to \infty$, and may be expressed in spherical polar coordinates as

$$v^{\pm}(r) = \mp r \frac{(\pm\cos\theta)^{1/2}\sin\theta}{1+\cos^{1/2}\theta}. \tag{44}$$

The associated dimensionless tangential stresses at the upper (+) and lower (−) sphere surface are given by

$$\tau^{\pm}_{r\theta}(\theta) = \pm E_k^{-1/2} \frac{\cos\theta\sin\theta}{1+(\pm\cos\theta)^{1/2}}, \tag{45}$$

$$\tau^{\pm}_{r\phi}(\theta) = -E_k^{-1/2} \frac{\cos\theta\sin\theta}{1+(\pm\cos\theta)^{1/2}}. \tag{46}$$

This stress field drives the $O(\epsilon)$ flow inside the drop. The form of the surface-stress-driven internal flow is deduced by a standard poloidal–toroidal decomposition, followed by a suitable eigenfunction expansion. The techniques employed are standard, and are outlined in Appendix C. The internal flow field is given by

$$\hat{u}_r(\bar{r},\theta) = -\sum_{l=1}^{\infty} B_l\, l(l+1)\,(\bar{r}^2-1)\,\bar{r}^{l-1}\,P_l(\cos\theta), \tag{47}$$

$$\hat{u}_\theta(\bar{r},\theta) = \sum_{l=1}^{\infty} B_l[(l+3)\,\bar{r}^{l+1}-(l+1)\,\bar{r}^{l-1}]\,P_l^1(\cos\theta), \tag{48}$$

$$\hat{u}_\phi(\bar{r},\theta) = -\sum_{l=1}^{\infty} A_l\,\bar{r}^{l}\,P_l^1(\cos\theta), \tag{49}$$

where P_l are the Legendre polynomials, and $P_l^1 = -\partial P_l/\partial\theta$ are the associated Legendre polynomials of the first order. The coefficients A_l, B_l in the eigenfunction expansions are defined in terms of the surface stresses as

$$A_l = \frac{2l+1}{2l(l^2-1)} \int_0^{\pi} \tau_{r\phi}(\theta)\,P_l^1(\cos\theta)\sin\theta\,\mathrm{d}\theta, \tag{50}$$

$$B_l = \frac{2l+1}{4l(l+1)(l+1)(2l+3)} \int_0^{\pi} \tau_{r\theta}(\theta)\,P_l^1(\cos\theta)\sin\theta\,\mathrm{d}\theta. \tag{51}$$

Poloidal surface stresses drive purely poloidal internal flows ($\hat{u}_\phi = 0$), and toroidal stresses drive purely toroidal flows ($\hat{u}_\theta = \hat{u}_r = 0$). The form of the internal flow is determined by substituting (45) and (46) into (47)–(51) and truncating the series at sufficiently large l, and is illustrated in figure 10. As viewed from above the rising drop, the internal flow is characterized by swirling toroidal flows in the clockwise and counterclockwise sense, respectively, above and below the drop equator. The poloidal flow is characterized by a circulation pattern reminiscent of the Hadamard–Rybczyński solution for a high-viscosity drop translating in an unbounded Stokes flow: fluid is

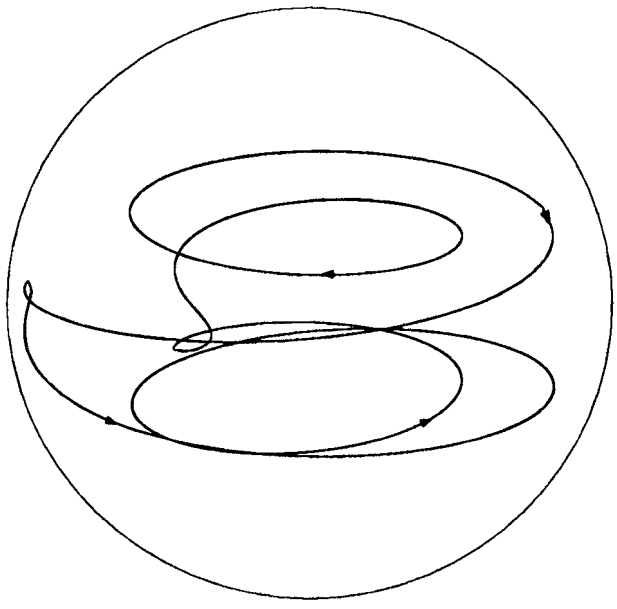

FIGURE 10. A single streamline illustrating the form of the flow induced within a high-viscosity ('Stokes') drop rising along the length of a Taylor column. The internal circulation is driven by the tangential stresses associated with the Ekman layer on the drop surface.

swept around the drop surface, and rises vertically near the drop's centre. The opposite sense of poloidal circulation relative to the geostrophic drop will be discussed in §7.

5. The unbounded problem

When a particle rises through an unbounded domain, the nature of the flow induced is entirely different from that in the bounded geometry. Fluid transport from the fore to the aft column regions occurs by viscous relaxation of the Taylor–Proudman constraint in vertical shear layers (figure 1), rather than through Ekman transport over the particle and container surfaces. The swirl velocities generated within the Taylor slug are comparable in magnitude to the rise speed: $U_s \approx U$. Balancing the characteristic geostrophic drag, of order $\rho\Omega U\pi R^3$, with the buoyancy force yields a steady rise speed U given by

$$U = \frac{3}{16}\frac{V}{R^3}\frac{\Delta\rho}{\rho}\frac{g}{\Omega}. \tag{52}$$

The coefficient $3\pi/16$ is included so that U corresponds precisely to the rise speed of a rigid axisymmetric body of revolution of equatorial radius R, as calculated by Moore & Saffman (1969). The rise speed decreases with increasing rotation rate, but is independent of the fluid viscosity. Since the particle's motion no longer relies explicitly on Ekman transport over the drop surface, the drag on the particle is independent of the detailed structure of the boundary layer on the drop surface. Consequently, the rise speed is independent of the particle's detailed shape, and depends only on its equatorial radius.

The physical picture of drop motion through an unbounded flow is changed very little by the presence of finite drop viscosity. We have demonstrated that in general the fluid viscosity prescribes the efficiency of Ekman transport over the drop surface, and

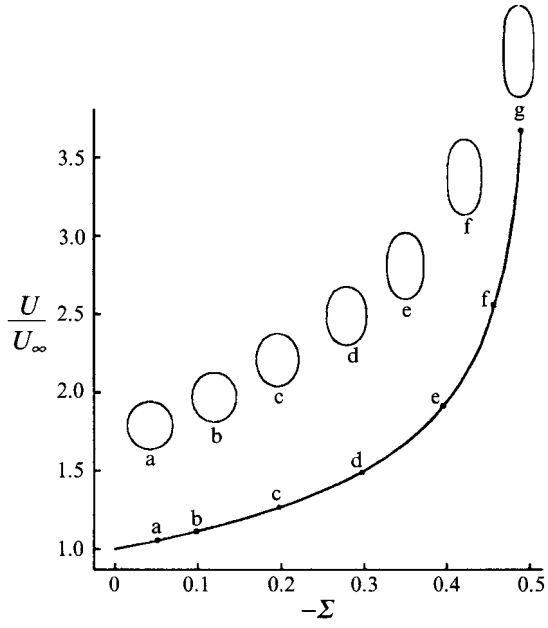

FIGURE 11. Rise speed and shape of a fluid drop bound by surface tension and rising on-axis through an unbounded flow, as a function of the rotational Bond number Σ. The rise speeds are normalized with respect to that of a spherical drop, $U_\infty = \frac{1}{4}\pi(\Delta\rho/\rho)(g/\Omega)$, and deformed shapes are scaled such that the volumes correspond to that of the undeformed spherical drop.

that this transport is always less than that over an equivalently shaped rigid particle. We thus conclude that, as in the rigid particle case, Ekman transport over a viscous drop rising through an unbounded fluid is negligible. The drop's rise speed corresponds to U, which depends only on the equatorial radius of the drop, which sets the maximum radius of the associated Taylor slug. We thus deduce the rise speed of a drop of known volume as a function of the rotational Bond number, which uniquely prescribes the drop's equatorial radius. The result is illustrated in figure 11.

6. Experiments

We proceed by presenting results of an experimental study of axial drop motion through a rapidly rotating plane layer of fluid bounded above and below by rigid horizontal boundaries. In addition to describing a number of qualitative features of the flow field, we quantify the dependence of rise speed on fluid depth and drop viscosity. Further details regarding these experiments, in addition to an experimental study of the effectively unbounded geometry, may be found in Bush (1993).

6.1. *Experimental technique*

Figure 12 illustrates the rotating tank apparatus and drop release mechanism designed and constructed for the experimental component of our study. The tank is rotated by a direct-drive system capable of sustaining angular speeds of 60 r.p.m. The rotating frame is coupled electrically to the laboratory frame through eight brush contacts mounted on the rotating axle. The tank consists of a 90 cm long Plexiglas cylinder of inner diameter 30.5 cm. A false lid is attached with a threaded screw so that its height can be adjusted, and the rise distance of the drops may thus be varied from 8 to 80 cm.

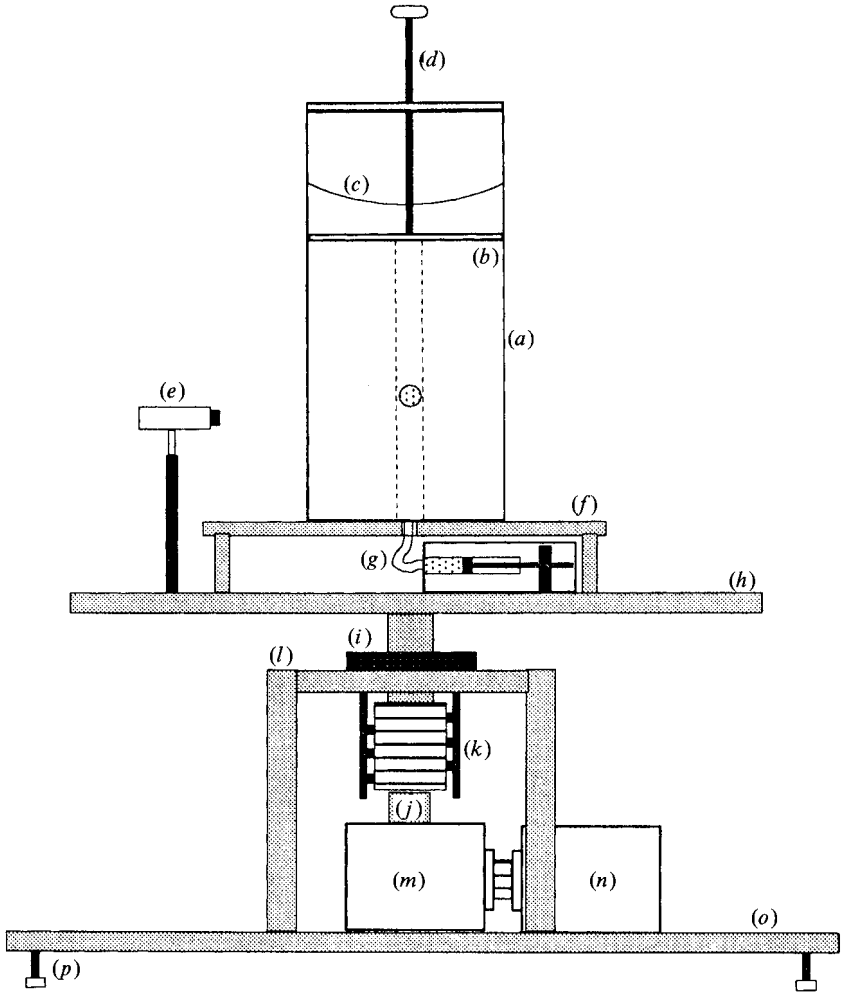

FIGURE 12. The rotating tank apparatus: (*a*) Plexiglas tank, (*b*) false lid, (*c*) free surface, (*d*) threaded screw, (*e*) video camera, (*f*) tank support frame, (*g*) release mechanism, (*h*) rotating base plate, (*i*) bearing, (*j*) axle, (*k*) brush contacts, (*l*) support structure, (*m*) gear box, (*n*) motor, (*o*) base plate, (*p*) levelling screws.

Drops of typical volume 35 ml are released from a 60 ml syringe driven by a linear actuator with a variable speed control.

A number of practical difficulties arose from the fact that the drop fluid has to be injected into the tank. The injection of drop fluid on-axis necessitates the ejection of water through the circular collar around the false lid; consequently, a source–sink flow corresponding to a geostrophic $1/r$ vortex (Hide 1968) is generated within the bulk of the fluid. Moreover, the inability to close the system enabled communication between the upper free surface and the fluid bulk; more specifically, the generation of inertial waves by surface waves. The false lid was designed with the intention of shielding the surface waves from the tank interior by viscous damping in the thin (1 mm) gap separating the lid from the tank walls. Finally, the on-axis release of the drop fluid alters the lower boundary condition on the flow. In particular, the lower surface does not correspond to a rigid horizontal boundary, but rather to an axisymmetric curved fluid–fluid interface.

Requirement	Ensures that	Reference
$E_k \ll 1$	viscous effects are confined to thin boundary layers	e.g. Greenspan (1968)
$\mathscr{R}_o \ll 1$	inertial effects associated with vertical motion are negligible	Moore & Saffman (1968)
$L \leqslant \frac{1}{10} R/E_k$	Taylor column spans entire fluid depth	Maxworthy (1968)
$\mathscr{R}_o/E_k^{1/2} \ll 1$	inertial effects associated with geostrophic swirling motions are negligible	Moore & Saffman (1969)
$\mathscr{R}_o/E_k^{3/7} \ll 1$	inertial effects in Stewartson layers are negligible	Moore & Saffman (1969)

TABLE 2. Summary of the desired parameter regime

Table 2 summarizes the restrictions which must be met in order to achieve the desired geostrophic parameter regime. The inertial effects associated with the vertical drop motion are typically small in our experiments ($\mathscr{R}_o \ll 1$); however, the inertial influences associated with the swirling motions within the Taylor column are not so easily neglected. In order to achieve swirl Rossby numbers $\mathscr{R}_o^s < 1$ in the laboratory, the normalized density defect, $\Delta\rho/\rho$, of the drop has to be less than 1%. Furthermore, if the density defect of the drop is less than 0.3%, the drop tends to wander off-axis. Consequently, the desired parameter regime can be achieved only with $0.3\% < \Delta\rho/\rho < 1.0\%$. Finally, the most stringent requirement, $\mathscr{R}_o/E_k^{3/7} \ll 1$ (Moore & Saffman 1969), is seldom met in the laboratory experiments; consequently, wave-like disturbances are often observed in the Stewartson layers.

Various Dow Corning silicone oils are used as the drop fluid, while the suspending fluid is either water or a water–ethanol solution. The interfacial tension of the silicone oil in water, typically 30 dyne cm^{-1} (Rumscheidt & Mason 1961), is sufficiently high that the drops are nearly spherical (with length to diameter ratio of less than 1.1). We denote the spherical drop radius by a. The observed rise speeds may thus be compared directly to the theoretical results for spherical drops summarized in figure 8. The principal source of error in the reported values of the normalized rise speed is the indeterminacy in the density defect, $\Delta\rho/\rho$, which arises from the necessity of matching very closely the densities of the drop and suspending fluids.

The density and viscosity of both the drop and suspending fluids are measured using standard hydrometers and glass capillary viscometers. A video image of a reference grid submerged in the tank is captured before each run. The tank is set in motion and the suspending fluid left to spin up. The drop fluid is injected slowly so as to minimize the excitation of inertial waves and pronounced source–sink flows. The drop's subsequent rise is recorded on video along with a time code image. The drop's motion is reviewed on video over the captured background of the reference grid, so that both the steady shape and rise speed can be calculated. The drops typically assume near-spherical shapes and steady rise speeds after rising only a few drop diameters.

A number of standard visualization techniques were used to observe the qualitative features of the flow. The nature of the source–sink flow associated with the injection of the drop, and the time required for the fluid to spin up, were visualized with the Thymol Blue technique of Baker (1966). The nature of the wake and Taylor column could be observed in an unobtrusive fashion by injecting in advance of the drop a small volume of white tracer fluid (Kalliroscope). Finally, the presence of small air bubbles or other visible impurities (refer to figure 2) often made it possible to deduce the sense of bulk circulation within the drop.

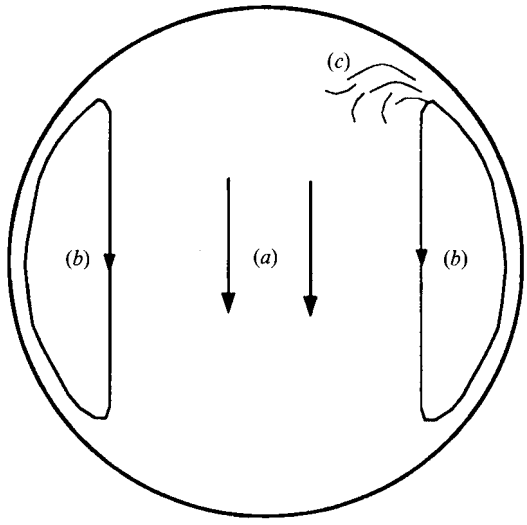

FIGURE 13. A schematic illustration of the flow observed within a spherical drop of viscosity 50 cS and radius 1.7 cm rising through water. The corresponding internal Ekman number is 3×10^{-3} and $\beta = 7.2$. The flow is characterized by regions of (*a*) slow downflow in the drop interior, (*b*) vigorous recirculation near the drop equator, and (*c*) instability of the recirculation eddies.

6.2. *Flow field observations, endwall and inertial effects*

Figure 13 illustrates the form of the flow observed inside the drop for $\beta = 7.2$, which is in qualitative agreement with that predicted by the geostrophic theory presented in §3. The internal motion is characterized by a bulk downward flow (relative to the drop surface), which is consistent with the presence of Ekman pumping and suction on, respectively, the upper and lower drop surfaces. The region of recirculation is confined to a thin region near the drop equator. The vigour of the recirculation was evident in an instability of the flow. It was impossible to observe the sense of internal circulation of the more sluggish flows induced inside the high-viscosity drops, as the convective timescale of the internal circulation was considerably greater than the rise time.

Figure 4 (plate 1) illustrates a drop rising in the bounded geometry (refer also to figures 2 and 3). The external flow structure is rendered visible by Kalliroscope, which is concentrated in the wake of the drop. The helical structure characteristic of the downstream Taylor column is also clearly visible. The corkscrew streamlines indicate the path followed by fluid as it is ejected from an Ekman layer then advected by the geostrophic swirl within the Taylor column. Indeed, the pitch of the helix gives an indication of the relative magnitudes of the vertical and swirling motions within the Taylor column (Maxworthy 1968).

Figure 14 illustrates the dependence of the normalized rise speed on a/L, the ratio of drop radius to rise distance. For this set of experiments, the drop radii were approximately 2 cm, and the height of the false lid was raised on successive runs. For $a/L \geqslant 0.08$, the rise speeds are constant; however, for small values of a/L, the speeds are seen to increase with rise distance. This observation indicates that the bounded results may be expected to obtain only for $a/L > 200E_k$, which is clearly a more stringent constraint than that proposed by Maxworthy (1968) and listed in table 2. This discrepancy is likely due to the persistence of inertial effects associated with the swirling motions within the column and the motions in the Stewartson layers.

Figure 15 illustrates the observed dependence of rise speed on the swirl Rossby

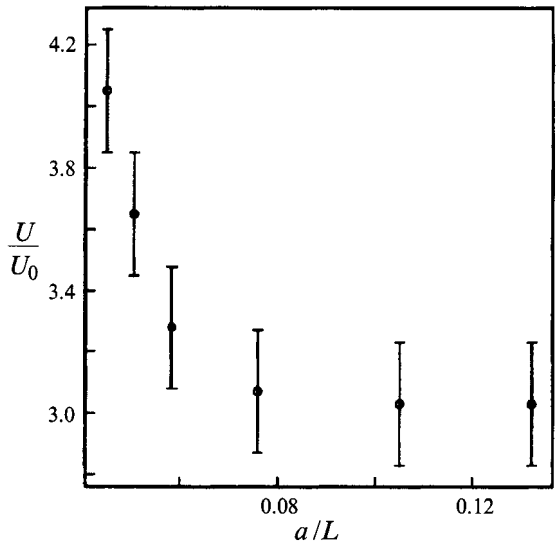

FIGURE 14. Data illustrating the dependence of rise speed on the ratio a/L, where a is the drop radius, and L is the depth of the fluid layer. Rise speeds are normalized with respect to the predicted value for a spherical bubble of the same size. For this set of experiments, $\beta = 10$.

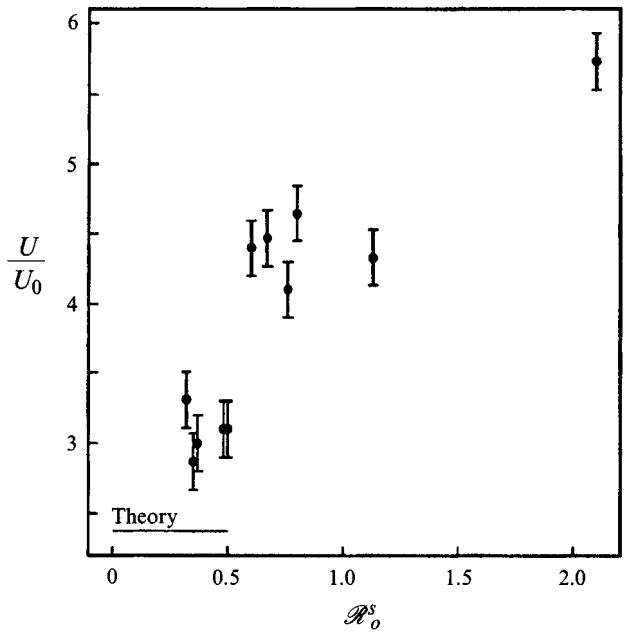

FIGURE 15. Data illustrating the dependence of rise speed on the swirl Rossby number, $\mathscr{R}_o^s$, for a series of runs with both $\beta = 23.3$ and $a/L = 0.1$ held constant. The solid line indicates the theoretically predicted value of 2.38 valid in the $\mathscr{R}_o^s \ll 1$ limit.

number for a series of runs made with $\beta = 23.3$. For this set of experiments, through blending silicone oils, we produced a series of drops with identical viscosities but varying densities. As the drop buoyancy decreases, and $\mathscr{R}_o^s$ decreases from a maximum of 2.1, the observed rise speeds steadily approach that predicted by theory. For $\mathscr{R}_o^s < 0.5$, the observed rise speeds were within roughly 25% of the value predicted on the basis of the geostrophic theory.

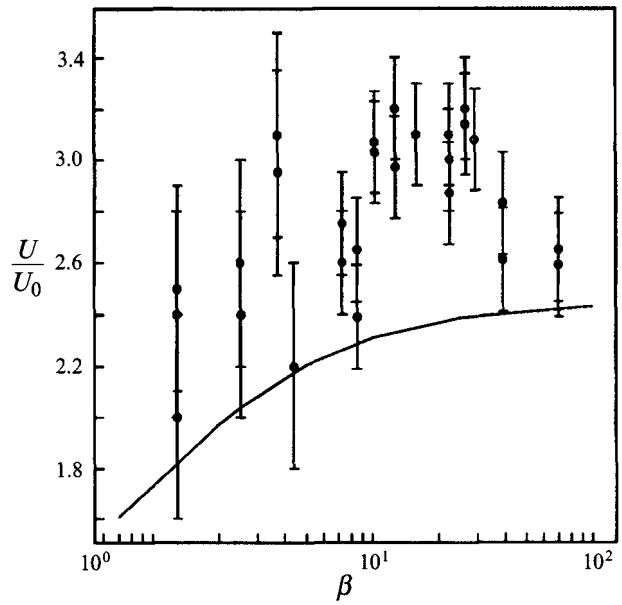

FIGURE 16. Experimental data illustrating the dependence of drop rise speed on $\beta = (\hat{\rho}/\rho)(\hat{\nu}/\nu)^{1/2}$. The rise speeds are normalized with respect to that of a spherical bubble between rigid boundaries. The solid curve indicates the theoretically predicted dependence of rise speed of a spherical drop between rigid horizontal boundaries, and corresponds to the upper curve of figure 8.

6.3. *The effects of drop viscosity*

Figure 16 illustrates the observed dependence of steady rise speed on the viscosity parameter β, along with the theoretically predicted dependence based on the assumption of a geostrophic spherical drop. Data for $\mathscr{R}_o^s < 0.5$ are presented. Runs for $\beta > 7$ were made using water as the suspending fluid, while the small-β regime was examined with ethanol–water suspending solutions. The errors in U/U_0 are larger at small β owing to the indeterminacies in the densities of the ethanol solutions, which arise from the development of weak stratification and preferential evaporation of the ethanol.

The ratio of internal to external fluid viscosities is seen to span four orders of magnitude. The internal Ekman number is small ($\hat{E}_k < 1$), so that the internal flow is expected to be geostrophic provided $\beta < 34$. In this range, roughly speaking, the normalized rise speeds increase monotonically with β in accordance with theory, but exceed the theoretically predicted values by up to 33%. For $\beta > 34$, the normalized rise speeds decrease, and so approach the rigid particle result, $U/U_0 = 105/43$, to within 10%.

The data presented in figure 16 all lie above the theoretical curve, and so indicate the importance of the inertial effects ignored in the theoretical development. The anomalously large rise speeds were likely associated with our inability to strictly satisfy the requirements $(\mathscr{R}_o^s, \mathscr{R}_o/E_k^{3/7}) \ll 1$. In accord with the observations of Maxworthy (1968), weak radial outflow driven by the inertia of the swirling fluid within the Taylor column may have facilitated the rise of the drop. Moreover, the observed inertial instabilities in the Stewartson layers may have contributed to the vertical transport in the Stewartson layers and so facilitated the rise of the drop.

Maxworthy (1968) noted that the observed rise speeds for rigid spheres between two rigid boundaries were in better agreement with theory than those of rigid spheres rising

beneath a free upper surface. This observation suggests that in the absence of an Ekman transport mechanism through which to efficiently transport fluid from the fore to the aft regions of the Taylor column, an alternative inertially dependent mechanism is favoured. Thus, as the drop viscosity decreases and the Ekman transport over the drop surface becomes less efficient, this boundary layer transport is obviated in favour of weak radial motions within the Taylor column. This reasoning might provide a possible explanation for the relative constancy of the rise speed over the wide range of β considered. An alternative explanation is that impurities in the base fluid aggregate on the drop surface in the form of surfactants and so act to rigidify the drop (e.g. Levich 1962). However, the observation of circulation within the drops in our experiments suggests that the effects of surfactants were not significant.

7. Discussion

Our theoretical analysis has yielded solutions for the steady shape and rise speed of a drop rising on-axis through a rapidly rotating fluid. The solutions for a variety of circumstances are summarized in table 3. While the rise speed is determined by a balance between hydrostatic and geostrophic pressures acting on the drop surface, the normal stress balance is to leading order independent of these pressure components, and the drop shape is set by a balance between centrifugal pressures and interfacial tension. Drop shapes correspond to prolate ellipsoids whose degree of distortion is determined by the rotational Bond number Σ. In the case of a drop rising through an unbounded fluid, the rise speed is independent of the fluid viscosities, and is uniquely prescribed by the rotational Bond number. In the bounded case, the rise speed further depends on the fluid viscosities, which prescribe the efficiency of Ekman transport over the drop and container boundaries.

The limits of high- and low-viscosity drops have been considered, and the forms of the internal flows demonstrated to be qualitatively different. Figure 17 illustrates schematically the form of the poloidal components of the flows induced inside spherical drops in which geostrophic and Stokes flows obtain. The flow within a Stokes drop is driven by tangential stresses associated with the Ekman layer on the drop surface. The poloidal flow is reminiscent of the Hadamard–Rybczyński solution for a Stokes drop translating in an unbounded fluid. As is evident in figure 10, however, the complete picture of the internal flow is complicated by a toroidal component corresponding to a swirling motion which reverses sense above and below the drop equator. The form of the flow induced inside a geostrophic drop is less intuitively obvious, but follows naturally from the Ekman pumping and suction induced by boundary layer flows in the curved double Ekman layer. It is interesting to speculate how the poloidal flow reverses sense as the internal Ekman number is increased and the internal flow changes from a geostrophic flow to a Stokes flow.

Our analysis of low-viscosity drops in bounded geometries may be applied to any possible combination of rigid or stress-free container boundaries. Moreover, we may extend our analysis to any problem in which geostrophic flows predominate and which is symmetric about the rotation axis; for example, the on-axis rise of n drops through a bounded fluid layer, and the on-axis motion of a drop through a system of n immiscible fluids whose interfaces are arbitrarily curved by centrifugal effects. The result of the calculation for the n-drop problem is listed in table 3.

Our experimental investigation has succeeded in demonstrating a number of the physical phenomena predicted to exist on the basis of theoretical considerations: Taylor slugs, Taylor columns, vigorous geostrophic swirling motions up- and

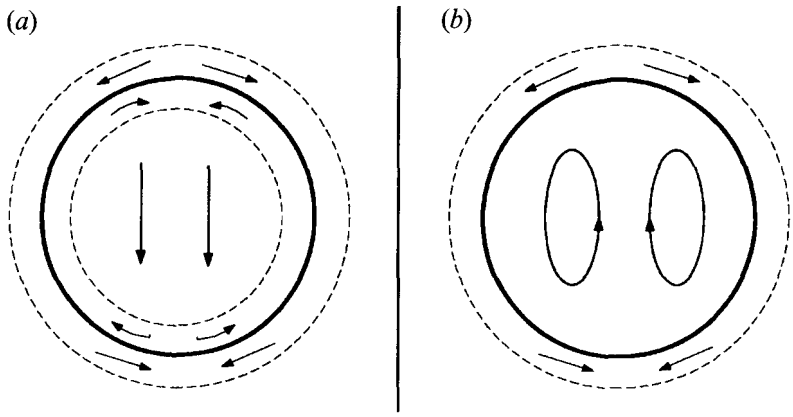

FIGURE 17. A schematic illustration of the poloidal flow components induced within (*a*) 'geostrophic' and (*b*) 'Stokes' drops rising along the length of a bounded Taylor column. Arrows within the Ekman layers denote the directions of net boundary layer transport. Note the opposite sense of circulation in the two cases.

Geometry	Rise speed	Prescribed by
Bounded (rigid boundaries)	$4U_0\left(\int_0^1 \frac{r^3\,\mathrm{d}r}{1+(1+f'^2)^{1/4}\beta/(1+\beta)}\right)^{-1}$	β, Σ
Bounded (free-slip or mixed boundaries)	$U_0\frac{4\beta}{1+\beta}\left(\int_0^1 \frac{r^3\,\mathrm{d}r}{(1+f'^2)^{1/4}}\right)^{-1}$	β, Σ
Unbounded	$\frac{3}{16}\frac{V}{R^3}\frac{\Delta\rho}{\rho}\frac{g}{\Omega}$	Σ
Bounded (n drops between rigid boundaries)	$4U_0 n\left(\int_0^1 \frac{r^3\,\mathrm{d}r}{1+(1/n)(1+f'^2)^{1/4}\beta/(1+\beta)}\right)^{-1}$	β, Σ, n

TABLE 3. A summary of theoretical predictions. U_0 is defined in equation (13)

downstream of the drop, Stewartson layers and Ekman layers. Most significantly, we have observed an internal circulation (illustrated in figure 13) consistent with the theoretically predicted planform (illustrated in figure 17) deduced on the assumption that the internal flow is geostrophic. The observed internal flow was characterized by a bulk downflow within the drop, and vigorous recirculation eddies in the vicinity of the drop equator. These observations are consistent with the theoretical description of the geostrophic drop presented in §3.

We have also observed a rich variety of phenomena neglected in the theoretical treatment of the problem: pronounced wall effects, fore–aft asymmetry in the flow associated with instabilities in the wake, helical wave-like instabilities in the Stewartson layers, and even instabilities in the internal motion. Most of these phenomena were manifestations of inertial effects within the flow, whose persistence was the principal source of difficulty in our experimental investigation.

This work has been supported by NSF Grants EAR-88-04618 and EAR-90-18620. HAS gratefully acknowledges support from NSF-Presidential Young Investigator Award, CTS-8957043. J.B. has also been supported by NSF-Presidential Young

Investigator Award EAR-91558298 and by a fellowship from the David and Lucille Packard Foundation.

We acknowledge Dr John D. Sherwood for a number of insightful suggestions concerning the double Ekman layer analysis and Professor Howard Emmons for several helpful conversations. We are also indebted to Jack Whitehead, Bob Fraezel and Ed Bolton for their consultation on the design of the experimental apparatus. Finally, we thank Philip Hartley, Jason Adams and Mike O'Connor for their assistance with the experiments.

Appendix A. Near sphere distortions of a bubble

In this section, we illustrate the first effects of the hydrostatic and geostrophic pressures on the drop shape through a perturbation analysis for a nearly spherical bubble. For the case of a spherical bubble rising between rigid horizontal boundaries, the swirling motions within the Taylor column take a particularly simple form, $v^{\pm}(r) = \mp Ur/\delta$ in dimensional variables, and (8) reduces to the form

$$(\hat{p}_0 - p_0) - \Delta\rho \tfrac{1}{2}\Omega^2 r^2 + \Delta\rho g z \mp \rho\Omega U r^2/\delta = \sigma \nabla_s \cdot \boldsymbol{n}. \tag{A 1}$$

Both the third and fourth terms on the left-hand side of (A 1), which correspond to the contributions of, respectively, the hydrostatic and geostrophic pressures, reverse sign at the equatorial plane $z = 0$. These pressures act to destroy the fore–aft symmetry of the bubble. Non-dimensionalizing all lengths with respect to the equatorial radius R (r and z henceforth denote dimensionless distances) and using (36) for the appropriate rise speed $U(\beta = 0)$ reduces (A 1) to the dimensionless form

$$P + 4\Sigma r^2 + \mathscr{G} z \mp \tfrac{4}{3}\mathscr{G}(a/R)^3 r^2 = \nabla_s \cdot \boldsymbol{n}, \tag{A 2}$$

where $\mathscr{G} = R^2 g \Delta\rho/\sigma$ and $\Sigma = -R^3\Omega^2\Delta\rho/8\sigma$ are, respectively, the gravitational and rotational Bond numbers, $P = (\hat{p}_0 - p_0)R/\sigma$, and a is the undeformed bubble radius. In the limit of $\mathscr{G}/\Sigma \ll 1$, the bubble again assumes the form of a prolate ellipsoid; however, in general both hydrostatic and geostrophic pressures must be considered.

We proceed by transforming into spherical coordinates $(\bar{r}, \theta, \phi)$, and writing (A 2) as

$$P + 4\Sigma \bar{r}^2 \sin^2\theta + \mathscr{G}\bar{r}\cos\theta \mp \tfrac{4}{3}\mathscr{G}(a/R)^3 \bar{r}^2 \sin^2\theta = \nabla_s \cdot \boldsymbol{n}. \tag{A 3}$$

In the limit of $\Sigma = \mathscr{G} = 0$, the bubble assumes a spherical form. We seek the form of the first aspherical perturbations, and so expand:

$$\bar{r} = 1 + \Sigma f(\theta) + \mathscr{G} g(\theta) + O(\Sigma^2, \mathscr{G}^2, \Sigma\mathscr{G}, \ldots), \tag{A 4}$$

$$P = P_0 + \Sigma P_1 + \mathscr{G} P_2 + O(\Sigma^2, \mathscr{G}^2, \Sigma\mathscr{G}, \ldots), \tag{A 5}$$

$$\nabla_s \cdot \boldsymbol{n} = 2 - \Sigma\mathscr{L} f(\theta) - \mathscr{G}\mathscr{L} g(\theta) + O(\Sigma^2, \mathscr{G}^2, \Sigma\mathscr{G}, \ldots), \tag{A 6}$$

where $(\Sigma, \mathscr{G}) \ll 1$, and the operator $\mathscr{L} \equiv \mathrm{d}/\mathrm{d}\theta^2 + \cot\theta\, \mathrm{d}/\mathrm{d}\theta + 2$. Equating terms of like powers yields

$$O(1): \quad P_0 = 2, \tag{A 7}$$

$$O(\Sigma): \quad \mathscr{L} f(\theta) + 4\sin^2\theta + P_1 = 0, \tag{A 8}$$

$$O(\mathscr{G}): \quad \mathscr{L} g(\theta) + \cos\theta \mp \tfrac{4}{3}\sin^2\theta + P_2 = 0. \tag{A 9}$$

Solving the ordinary differential equations for $f(\theta)$ and $g(\theta)$ and requiring that the drop volume be conserved yields $P_1 = -2$, $P_2 = 0$, and solutions for the drop shape:

upper surface $(0 < \theta < \pi/2)$:

$$\bar{r}(\theta) = 1 + \Sigma(\tfrac{1}{3} - \cos^2\theta) + \mathscr{G}(\tfrac{1}{3}\cos\theta \log(1 + \cos\theta) + \tfrac{1}{3}\cos^2\theta) + \ldots; \tag{A 10}$$

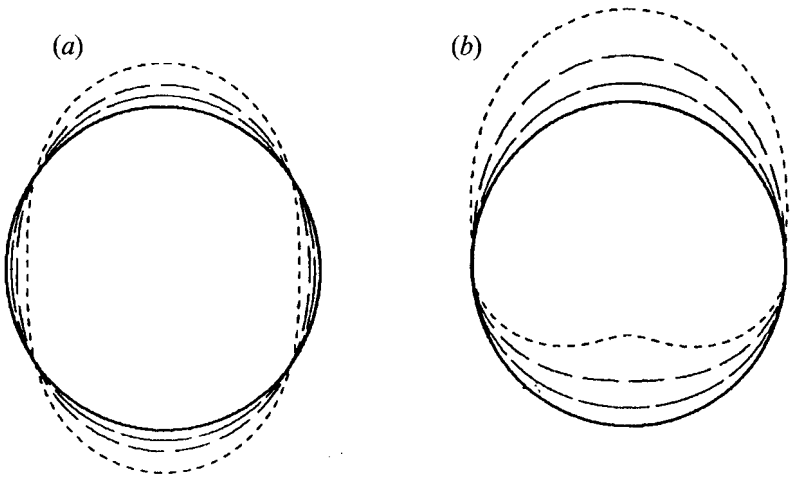

FIGURE 18. Results of a perturbation analysis of a nearly spherical bubble rising along the length of a Taylor column bounded above and below by rigid horizontal boundaries. (*a*) The first effects of rotation on a bubble when $\mathscr{G}$ is set to zero, and Σ decreases through the range $(0, -0.1, -0.2, -0.4)$. (*b*) The first effects of geostrophic and hydrostatic pressures for $\Sigma = 0$ when $\mathscr{G}$ increases through the range (0, 0.2, 0.5, 1.0).

lower surface $(\pi/2 < \theta < \pi)$:

$$\bar{r}(\theta) = 1 + \Sigma(\tfrac{1}{3} - \cos^2\theta) + \mathscr{G}(\tfrac{1}{3}\cos\theta \log(1 - \cos\theta) - \tfrac{1}{3}\cos^2\theta) + \ldots. \tag{A 11}$$

As illustrated in figure 18, the first effect of rotation (finite Σ) is once again to distort the bubble into a prolate ellipsoid. The first effect of the combined hydrostatic and geostrophic pressures (finite $\mathscr{G}$) is to break the bubble's fore–aft symmetry through distorting it into a bullet shape.

Appendix B. Ekman compatibility conditions: a review

When an $O(1)$ geostrophic swirling flow $v(r)$ is disrupted from below by a rigid axisymmetric boundary with a shape prescribed by $z = f(r)$, radial gradients in the radial Ekman layer flux necessitate a weak $O(E_k^{1/2})$ vertical flow into or out of the boundary layer of magnitude

$$w(r) = \frac{E_k^{1/2}}{2r}\frac{\mathrm{d}}{\mathrm{d}r}(rv(r)[1 + f'^2]^{1/4}), \tag{B 1}$$

where $f' = \mathrm{d}f/\mathrm{d}r$ and all variables are dimensionless. In §3, Ekman compatibility conditions are required at rigid ($c = 1$) and stress-free ($c = 0$) horizontal boundaries ($f' = 0$). In this case, (B 1) reduces to the form

$$w(r) = c\frac{E_k^{1/2}}{2r}\frac{\mathrm{d}}{\mathrm{d}r}(rv(r)). \tag{B 2}$$

A stress-free surface ($c = 0$) does not disrupt the overlying swirling flow; consequently, no Ekman layer need exist at the boundary, and no Ekman pumping or suction is generated by the presence of the boundary.

When geostrophic swirling motions occur in immiscible fluids adjoined by an axisymmetric interface with a shape prescribed by $z = f(r)$, the boundary layer at the

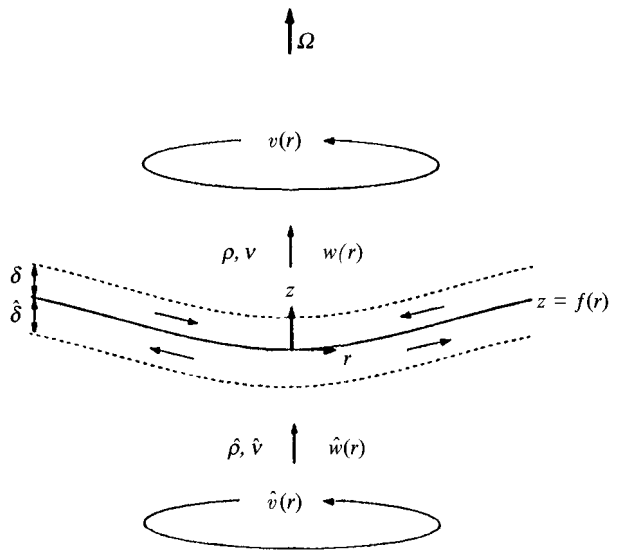

FIGURE 19. A schematic illustration of a double Ekman layer. Arrows in the boundary layers denote the directions of net boundary layer flux for the case of $v(r) > \hat{v}(r)$.

fluid–fluid interface assumes the form of a curved double Ekman layer (illustrated in figure 19). The geostrophic swirling flows above and below the interface, respectively $v(r)$ and $\hat{v}(r)$, are disrupted by viscous effects in the neighbourhood of the interface. Matching tangential velocities and stresses at the interface and applying the appropriate far-field boundary conditions yields a solution for the boundary layer flows which correspond to modified Ekman spirals. The interface has a swirling velocity $v_{int}(r)$ whose magnitude is between $v(r)$ and $\hat{v}(r)$:

$$v_{int}(r) = \frac{1}{1+\beta} v(r) + \frac{\beta}{1+\beta} \hat{v}(r), \tag{B 3}$$

where $\beta = (\hat{\rho}/\rho)(\hat{\nu}/\nu)^{1/2}$ is the viscosity ratio parameter characterizing the two fluids. The detailed solution indicates that, while the interface has a swirling component to its motion, there is no meridional motion along the interface. This feature reflects that the Ekman boundary layer flows are driven by pressure gradients of opposite sense above and below the interface. Tangential gradients in the tangential boundary layer fluxes necessitate weak vertical fluxes into or out of the boundary layer of magnitude

$$w(r) = \frac{\hat{\rho}}{\rho} \hat{w}(r) = \frac{\beta}{1+\beta} \frac{E_k^{1/2}}{2r} \frac{\mathrm{d}}{\mathrm{d}r} (r(v(r) - \hat{v}(r)) [1 + f'^2]^{1/4}). \tag{B 4}$$

This result is valid only for smoothly varying functions $f(r)$, and breaks down if the variations of the interface occur over lengthscales comparable to the boundary layer thickness, or if the interface becomes vertical.

Appendix C. Surface-stress-driven motions in a Stokes sphere

We derive herein the form of the flow induced within a spherical fluid drop by axisymmetric tangential stresses $\tau_{r\theta}(\theta)$ and $\tau_{r\phi}(\theta)$ applied at its surface, when the drop dynamics may be described with Stokes equations. We express the axisymmetric

internal flow in spherical coordinates $(\bar{r}, \theta)$ in terms of poloidal and toroidal scalar functions (e.g. Backus 1986), respectively $T(\bar{r}, \theta)$ and $P(\bar{r}, \theta)$:

$$\hat{\boldsymbol{u}}(\bar{r}, \theta) = \boldsymbol{\nabla} \wedge \boldsymbol{\Lambda} P(\bar{r}, \theta) + \boldsymbol{\Lambda} T(\bar{r}, \theta) = \left(-\frac{\mathscr{L}^2 P}{\bar{r}}, -\frac{1}{\bar{r}} \frac{\partial}{\partial \bar{r}} \left(\bar{r} \frac{\partial P}{\partial \theta} \right), \frac{\partial T}{\partial \theta} \right), \tag{C 1}$$

where the vector operator $\boldsymbol{\Lambda} \equiv \boldsymbol{r} \wedge \boldsymbol{\nabla}$ and $\mathscr{L}^2 \equiv -(1/\sin\theta)(\partial/\partial\theta)(\sin\theta\,\partial/\partial\theta)$.

Substituting into Stokes equations (7) yields

$$\boldsymbol{\Lambda} \nabla^4 P + \boldsymbol{\nabla} \wedge \boldsymbol{\Lambda} \nabla^2 T = 0. \tag{C 2}$$

The radial component of (C 2) indicates that the toroidal scalar function T is harmonic, and the radial component of its curl that the poloidal scalar function P is biharmonic:

$$\nabla^2 T = 0, \quad \nabla^4 P = 0. \tag{C 3}$$

The toroidal and poloidal scalars may thus be expanded in terms of Legendre polynomials of order l:

$$T(\bar{r}, \theta) = \sum_{l=0}^{\infty} \left(A_l \bar{r}^l + \frac{B_l}{\bar{r}^{l+1}} \right) P_l(\cos\theta), \tag{C 4}$$

$$P(\bar{r}, \theta) = \sum_{l=0}^{\infty} \left(C_l \bar{r}^l + \frac{D_l}{\bar{r}^{l+1}} + E_l \bar{r}^{l+2} + \frac{F_l}{\bar{r}^{l-1}} \right) P_l(\cos\theta), \tag{C 5}$$

where A_l to F_l are constants. Application of the appropriate boundary conditions ($\hat{\boldsymbol{u}}$ finite at $r = 0$, $u_r = 0$ at $\bar{r} = 1$, and the surface stress conditions) yields the form of the internal flow given in equations (47)–(51).

REFERENCES

Backus, G. E. 1986 Poloidal and toroidal fields in geomagnetic field modeling. *Rev. Geophys.* **24**, 75–109.

Baker, J. 1966 A technique for the precise measurement of fluid flow in the range 0–5 cm/s. *J. Fluid Mech.* **26**, 573–575.

Baker, G. R. & Israeli, M. 1981 Spinup from rest of immiscible fluids. *Stud. Appl. Maths* **65**, 249–268.

Berman, A. S., Bradford, J. & Lundgren, T. S. 1978 Two-fluid spin-up in a centrifuge. *J. Fluid Mech.* **84**, 411–431.

Bush, J. W. M. 1993 Drop motion in rotating fluids: A model of compositional convection in the Earth's core. PhD thesis, Harvard University.

Bush, J. W. M., Stone, H. A. & Bloxham, J. 1992 The motion of an inviscid drop in a bounded rotating fluid. *Phys. Fluids* A **4**, 1142–1147.

Grace, S. F. 1926 On the motion of a sphere in a rotating liquid. *Proc. R. Soc. Lond.* A **113**, 46–77.

Greenspan, H. P. 1968 *The Theory of Rotating Fluids*. Cambridge University Press.

Hide, R. 1968 On source-sink flows in a rotating fluid. *J. Fluid Mech.* **32**, 737–764.

Hocking, L. M., Moore, D. W. & Walton, I. C. 1979 The drag on a sphere moving axially in a long rotating container. *J. Fluid Mech.* **90**, 781–793.

Levich, V. G. 1962 *Physicochemical Hydrodynamics*. Prentice-Hall.

Long, R. R. 1953 Steady motion around a symmetrical obstacle moving along the axis of a rotating fluid. *J. Met.* **10**, 197–203.

Maxworthy, T. 1968 The observed motion of a sphere through a short, rotating cylinder of fluid. *J. Fluid Mech.* **40**, 453–480.

Maxworthy, T. 1970 The flow created by a sphere moving along the axis of a rotating, slightly viscous fluid. *J. Fluid Mech.* **31**, 643–656.

MOORE, D. W. & SAFFMAN, P. G. 1968 The rise of a body through a rotating fluid in a container of finite length. *J. Fluid Mech.* **31**, 635–642.

MOORE, D. W. & SAFFMAN, P. G. 1969 The structure of free vertical shear layers in a rotating fluid and the motion produced by a slowly rising body. *Phil. Trans. R. Soc. Lond.* A **264**, 597–634.

MORRISON, J. W. & MORGAN, G. W. 1956 The slow motion of a disc along the axis of a viscous, rotating liquid. *Rep.* 56207/8. Div. of Appl. Maths, Brown University.

PRITCHARD, W. G. 1969 The motion generated by a body moving along the axis of a uniformly rotating fluid. *J. Fluid Mech.* **39**, 443–464.

PROUDMAN, J. 1916 On the motion of solids in a liquid possessing vorticity. *Proc. R. Soc. Lond.* A **92**, 408–424.

ROSENTHAL, D. K. 1962 The shape and stability of a bubble at the axis of a rotating liquid. *J. Fluid Mech.* **12**, 358–366.

ROSS, D. K. 1968*a* The shape and energy of a revolving liquid mass held together by surface tension. *Austral. J. Phys.* **21**, 823–835.

ROSS, D. K. 1968*b* The stability of a revolving liquid mass held together by surface tension. *Austral. J. Phys.* **21**, 837–844.

RUMSCHEIDT, F. D. & MASON, S. G. 1961 Particle motions in sheared suspensions XII. Deformation and burst of fluid drops in shear and hyperbolic flow. *J. Colloid Sci.* **16**, 238–261.

STEWARTSON, K. 1952 On the slow motion of a sphere along the axis of a rotating fluid. *Proc. Camb. Phil. Soc.* **48**, 168–177.

STEWARTSON, K. 1953 On the slow motion of an ellipsoid in a rotating fluid. *Quart. J. Mech. Appl. Math.* **6**, 141–162.

STEWARTSON, K. 1958 On the motion of a sphere along the axis of a rotating fluid. *Quart. J. Mech. Appl. Math.* **11**, 39–51.

TAYLOR, G. I. 1917 Motion of solids in fluids when the flow is not irrotational. *Proc. R. Soc. Lond.* A **93**, 99–113.

TAYLOR, G. I. 1921 Experiments with rotating fluids. *Proc. R. Soc. Lond.* A **100**, 114–121.

TAYLOR, G. I. 1922 The motion of a sphere in a rotating liquid. *Proc. R. Soc. Lond.* A **102**, 180–189.

TAYLOR, G. I. 1923 Experiments on the motion of solid bodies in rotating fluids. *Proc. R. Soc. Lond.* A **104**, 213–219.

VONNEGUT, B. 1942 Rotating bubble method for the determination of surface and interfacial tensions. *Rev. Sci. Instrum.* **13**, 6–9.